Application of GNSS Interferometric Reflectometry for Lake Ice Studies

by

Yusof Ghiasi

A thesis
presented to the University of Waterloo
in fulfillment of the
thesis requirement for the degree of
Master of Science
in
Geography

Waterloo, Ontario, Canada, 2020

Author's Declaration

I hereby declare that I am the sole author of this thesis. This is a true copy of the thesis, including any required final revisions, as accepted by my examiners.

I understand that my thesis may be made electronically available to the public.

Abstract

This thesis examines the use of Global Navigation Satellite System Interferometric Reflectometry (GNSS-IR) for the study of lake ice with a particular focus on the estimation of ice thickness. Experiments were conducted in two lake regions: (1) sub-Arctic lakes located near Yellowknife and Inuvik in the Northwest Territories during March 2017 and 2019, and (2) MacDonald Lake, Haliburton, Ontario, which is known as a mid-latitude lake, during the ice season of 2019-2020. For both regions, GNSS-IR results are compared and validated against in-situ ice and on-ice snow measurements, and also with ice thickness derived from thermodynamic lake ice models. In the first experiment, GNSS antennas were installed directly on the ice surface and the ice thickness at each site was estimated by analyzing the signal-to-noise ratio (SNR) of the reflected GNSS signals. The GNSS-IR capability of ice thickness estimation tested on sub-Arctic lakes results in a root mean square error (RMSE) of 0.07 m, a mean bias error (MBE) of -0.01 m, and a correlation of 0.66. At MacDonald Lake, a GNSS antenna was mounted on a 5-m tower on the shore to collect reflected signals from the lake surface. The Least-Squares Harmonic Estimation (LS-HE) method was applied to retrieve higher SNR frequencies in order to estimate the depths of multiple layers within lake ice and the overlaying snowpack. Promising results were obtained from this experiment; however, ice thickness estimation using GNSS-IR at this mid-latitude lake site was found to be highly dependent on the presence or absence of wet layers such as slush at the snow-ice interface and wet snow above that interface. On colder days, when there was a lower chance for the formation of wet layers, ice thickness could be estimated with a correlation of 0.68, RMSE of 0.07 m, and MBE of -0.02 m. In addition, GNSS-IR showed the potential for determining the freeze-up and break-up timing based on the SNR amplitude of reflected signals. The novel work presented in this thesis points to the potential of using reflected

signals acquired by recent (e.g. Cyclone Global Navigation Satellite System (CYGNSS) and TechDemoSat-1 (TDS-1)) and future GNSS-R missions for lake ice investigations.

Acknowledgement

I would like to express my deepest gratitude to my supervisor, Professor Claude Duguay, for giving me the opportunity to work on this exciting research as one of the Transformative sensor Technologies and Smart Watersheds (TTSW) projects. I would also like to thank him for all the experiences I gained through fieldwork trips and national conferences as his graduate student. Creating an enjoyable and unique workplace for his students, Claude has been continuously providing me with invaluable feedback and advice throughout the completion of this work. Words are too powerless to express my sincere appreciation to his scientific, moral, and financial supports.

This journey would not complete without a close collaboration with Claude's group members, especially Justin Murfitt, Marie Hoekstra, and Amir Masoud Chegoonian, who provided me with their warm and unfailing supports from the very beginning days. I will never forget their friendly helps to a fresh student who just entered a very new environment.

I would also like to acknowledge the financial support from Global Water Future (GWF) for this research. In addition, I would like to thank Dr. Laura Brown, from the University of Toronto, and her professional team for sharing their meteorological data with us. Moreover, I would like to thank the management and staff members of the Haliburton Forest and Wildlife Reserve for providing us with their permission and support to conduct the big part of this thesis at the MacDonald Lake beach.

Lastly, I would like to thank my beloved wife, Tayebe, for her incessant support and exceptional patience. She spared no efforts to make this journey as easy as it could ever been. I would also like to extend thanks to all friends for their continued supports.

Table of Contents

List of Figures

Chapter 1 –Introduction

1.1. Motivation

Lakes that form a seasonal ice cover can have a significant impact on regional weather and climate in lake-rich regions as they play a vital role in the transfer of heat and moisture to atmosphere. In addition, cultural ecosystem, which includes ice fishing and winter transportation via ice roads, and recreational activities such as snowmobiling, are highly dependent on the timing and duration of ice cover as well as ice thickness (Brown & Duguay, 2010; Knoll et al., 2019). However, studies have shown a significant decrease in ice duration for northern lake-ice covers over the past 150 years and predict that this downturn will continue in the foreseeable future (Benson et al., 2012; Brown & Duguay, 2010; Duguay et al., 2006; Rouse et al., 2008). This trend poses a serious threat to aquatic ecosystems and the economy of northern countries (Prowse et al., 2011). Therefore, there is a pressing need to map/monitor lake ice characteristics, such as ice duration and ice thickness, from satellite measurements since government programs supporting ground-based ice observations in countries like Canada have been severely eroded since the1990s (Duguay et al., 2006; Lenormand et al., 2002).

Employing optical and microwave remote sensing techniques, researchers have made some progress on the mapping/monitoring of lake ice extent, ice phenology and ice thickness as well as describing ice properties that have an impact on reflected/emitted signals (Duguay et al., 2015). Investigations have shown a strong correlation (>0.90) between satellite/ground-based microwave systems estimates of ice thickness and field measurements (e.g., Gunn et al., 2015; Kang et al., 2010). In addition, methods using thermal remote sensing data have shown good potential for the retrieval of ice thickness with correlations and errors (RMSE of less than 20 cm) of the same order

of magnitude to those reported from microwave approaches (e.g., Kheyrollah Pour et al., 2012; Murfitt et al., 2018). However, the quality of data acquired by the above-mentioned systems are either dependent on weather conditions (e.g. thermal) or acquired at coarse spatial resolutions (e.g., tens of km for passive microwave sensors). Also, ground-based radar systems (e.g., Gunn et al., 2015) are too expensive (several hundred thousands of dollars) to acquire and operate at several sites.

Meanwhile, the multipath signals of Global Navigation Satellite System (GNSS) have shown some potential, though very limited to date, for lake ice studies. This technique, which is known as GNSS Interferometric Reflectometry (GNSS-IR), can be employed as a low-cost remote sensing solution. GNSS-IR is an "active-passive" method in which a GNSS antenna (e.g., a geodetic GPS receiver) deployed on land receives signals transmitted by GNSS satellites and reflected off the surrounding area of the antenna. The term "Interferometric" is used because both direct line-of-sight and reflected signals are acquired by a single GNSS antenna, and an interferometric pattern is achieved (see Chapter 2 for details). GNSS signals are classified as L-band (1-2 GHz frequency range); therefore, in GNSS-IR, the signature of the reflective surface at L-band wavelength is the matter of concern.

Known as a ground-breaking technique for studying hydrologic and cryospheric variables at the local scale, such as soil moisture (e.g., Chew et al., 2016; Vey et al., 2016), snow depth (e.g., Larson, 2016), and ground displacement in permafrost regions (e.g., Liu & Larson, 2018; Wu et al., 2018), the potential of GNSS-IR has only been briefly touched upon for estimating lake ice thickness (Jacobson, 2015). Furthermore, the technique has been discussed as a tool for sea ice detection (Strandberg et al., 2017) and for estimating snow accumulation on the Greenland Ice Sheet (GIS) (Larson et al., 2020).

In contrast to GNSS-IR, there have been several studies employing more than one GNSS antenna facing two or more different directions (up, down, and sideways) to receive direct and reflected signals separately. This so-called GNSS reflectometry (GNSS-R) technique is employed on ground-based and, more recently, spaceborne platforms. For example, researchers have proposed ground-based GNSS-R to characterize dry-snow sub-structures (Cardellach et al., 2012), and have applied the technique for sea-ice phase-altimetry to reach height retrieval accuracies of about 3 cm (Fabra et al., 2011). Furthermore, spaceborne GNSS-R has been applied for ice and snow studies. TechDemoSat-1 satellite data have been used to detect melting of the GIS with a 90% agreement when compared to microwave radiometer measurements (Li et al., 2020). In addition, using NASA's Cyclone Global Navigation Satellite System (CYGNSS) micro-satellite level-0 raw data, researchers have demonstrated the capability of group delay altimetry with a sub-meter precision (Li et al., 2019), which points to the potential of estimating the lake ice thickness using CYGNSS altimetry, as recently proposed by Mayers & Ruf (2018) but yet to be fully demonstrated.

In general, multipath GNSS signals have so far shown some potential for studying ice and snow characteristics on freshwater lakes. However, the similar signature of snow and ice at L-band due to their low dielectric constant and contrast between dry layers (Engram et al., 2013) makes reflectometry studies to study snow on lake ice surfaces challenging but attractive to estimate ice thickness due to the large dielectric contrast between ice and water (i.e. ice-water interface). The potential of GNSS-IR has not yet been examined for studying neither sub-Arctic nor mid-latitude frozen lakes. While the technique may allow for ice thickness retrievals on lakes located in cold regions (e.g., Arctic and sub-Arctic), it may be more limited for retrievals at mid-latitude lake locations due to the impact of wetness at the top of the snowpack or within snow layers over ice

(including slushing at the snow-ice interface), a common situation observed due to mid-winter thaw events and the formation of snow ice. Such layers are worth noting because they present a high dielectric contrast compared to snow and ice, and have a similar signature to that of water on the L-band signals. Conducting GNSS-IR lake ice experiments at a mid-latitude location, in addition to the sub-Arctic, sheds further light on lake ice studies, including the timing of freeze-up and break-up period, as well as the ability of GNSS-IR in the detection/identification of the main reflective layers of snow-covered lake ice.

1.2. Research Objectives

The main goal of this research is to examine the ability of the GNSS-IR technique for the estimation of lake ice thickness covered by snow. Other properties of frozen lakes, such as freeze-up timing and slush detection are studied as well for a mid-latitude lake location. However, lake ice decay could not be investigated since the experiment was stopped at break-up due to the COVID-19 pandemic.

A GNSS-IR experiment was first conducted at several lake sites located between 63° N to 68° N (near Yellowknife and near Inuvik, Northwest Territories) to estimate lake ice thickness. In this experiment, GNSS antennas had not been initially deployed for reflectometry research but rather as ground control points for airborne and spaceborne synthetic aperture radar (SAR) campaigns. By deploying the antennas directly on the ice surface, however, we obtained promising results in the estimation of ice thickness which resulted in a short paper (Letter) submitted for publication in the journal *Remote Sensing* (Chapter 3 of this thesis). This is the first study of its kind to demonstrate the ability of the GNSS-IR technique for estimating of lake ice thickness at several lake locations in the sub-Arctic.

A second experiment was conducted on the southern shore of the MacDonald Lake, located in the Haliburton Forest and Wildlife Reserve, Haliburton, Ontario, Canada (78.56° W, 45.24° N). In this experiment, a dual-frequency GNSS receiver was installed on the shore at a height of 5-m above the lake surface to collect multipath GNSS signals during the 2019-2020 ice season. The depth of each contributing layer (i.e., snow, slush and ice) to the reflected signals was estimated through the analysis of signal-to-noise ratio (SNR) extracted from the GNSS-IR time series. Results were validated against in-situ measurements, snow data from the weather station located next to the GNSS receiver, Stefan's model for ice thickness estimation, and Canadian Lake Ice Model's (CLIMo) output including ice thickness and snow accumulation on the ice.

1.3. Thesis Outline

Chapter 2 provides general background information on lake ice phenology and ice growth, the principles of GNSS constellation and functioning, and the basics of interferometric reflectometry as a non-positioning application of GNSS in cold regions studies, as well as an overview on SNR time-series analysis methods. Chapter 3 presents the results of the GNSS-IR experiment for sub-Arctic lake ice covers in the form of a paper manuscript. Chapter 4 contains a description of the experimental setup at MacDonald Lake, a comparison between GNSS-IR results and other complimentary (field and model) data, and a discussion of the results. Chapter 5 summarizes the main findings of the study, the limitations of the experiments, and general directions for future research.

Chapter 2 –Background and Theory

The aim of this chapter is to provide the reader with some background and theoretical foundations of GPS/GNSS. It is divided into four sections: (1) a general introduction to lake ice formation and characteristics, (2) the principle of GPS as the most common GNSS, (3) the basics of GNSS-IR and its limited application thus far to lake ice studies, and (4) an overview on the analysis of SNR time-series, which is the salient data of the experimental results presented in Chapters 3 and 4.

2.1. Lake Ice

The phenology of lake ice is comprised by two main events, known as freeze-up and break-up periods, which cause an annual cycle for the formation and decay of lake ice covers. The timing of freeze-up and break-up is dominantly controlled by the local air temperature; however, other climatic and non-climatic factors, including altitude, elevation, lake morphometry, and precipitation have impacts on lake ice phenology. The general period between the freeze-up (fall and winter months) and break-up (spring months) is referred as ice season. For mid-latitude lakes, such as the MacDonald Lake, mid-winter thawing and refreezing are very common, which lead to the formation of multiple layers in an ice column. Since these layers may encompass different signatures on reflected GNSS signals, the physical characteristics of lake ice is expanded upon in subsequent sections.

2.1.1. Lake ice formation, growth and decay

The timing of both freeze-up and break-up is primarily controlled by the local air temperature, which determines the amount of heat absorbed by the lake (Williams, 1965). In the fall, once the temperature drops and water reaches its maximum density at 4^{o}C, an initial ice layer

forms on the surface that is called skim ice or black ice. Based on the size of the lake and the presence of wind, the freezing temperature varies so that the starting point for shallower lakes is 2-3^{o}C, whereas it is 1^{o}C for larger lakes (Jeffries et al., 2005). In contrast to black ice, which is congealed downward at the ice-water interface, white ice forms due to the presence of snow on the top of pre-formed ice, which leads to breaking (cracking of) the ice sheet below, allowing the water to flood on the ice surface[1], and creating a slush layer. Rapid freezing of the slush layer forms an opaque layer of ice called white ice or snow ice, and this process is likely to take place several times leading to multiple layers of slush and white ice. On the other hand, as temperature begins to rise in spring, the white ice layer melts, and the black ice absorbs more solar radiation, which accelerates the melting (Heron & Woo, 1994).

As shown in Figure 2.1., the black ice or congelation ice grows from the bottom of the ice column and the temperature gradient results in the conduction of the latent crystallization heat to the atmosphere (Stage 1). By accumulation of snow on the ice surface, the growth rate of ice decreases due to a decrease in the temperature gradient (Stage 2). The snow load, which is a function of snow depth and density (i.e., the snow mass), pushes the ice surface down and depresses it below the water equilibrium line. As a consequence, water flows up through cracks and soaks the base of the snowpack resulting in slush formation. At this stage, the black ice growth ceases since no temperature gradient happens in the ice (Stage 3). Heat conduction still continues through the snowpack; therefore, the slush layer freezes and forms a layer of snow-ice or white ice on the top of the ice column. In this stage, black ice growth resumes as the heat conduction resumes again through the ice and snow layers (Stage 4). This process repeats and causes forming more

[1] This flooding is not necessarily because of the ice breaking, but it also can be due to the snow melting.

slush and snow-ice layers on lakes experiencing frequent and large snow accumulations which depress the ice below the water line.

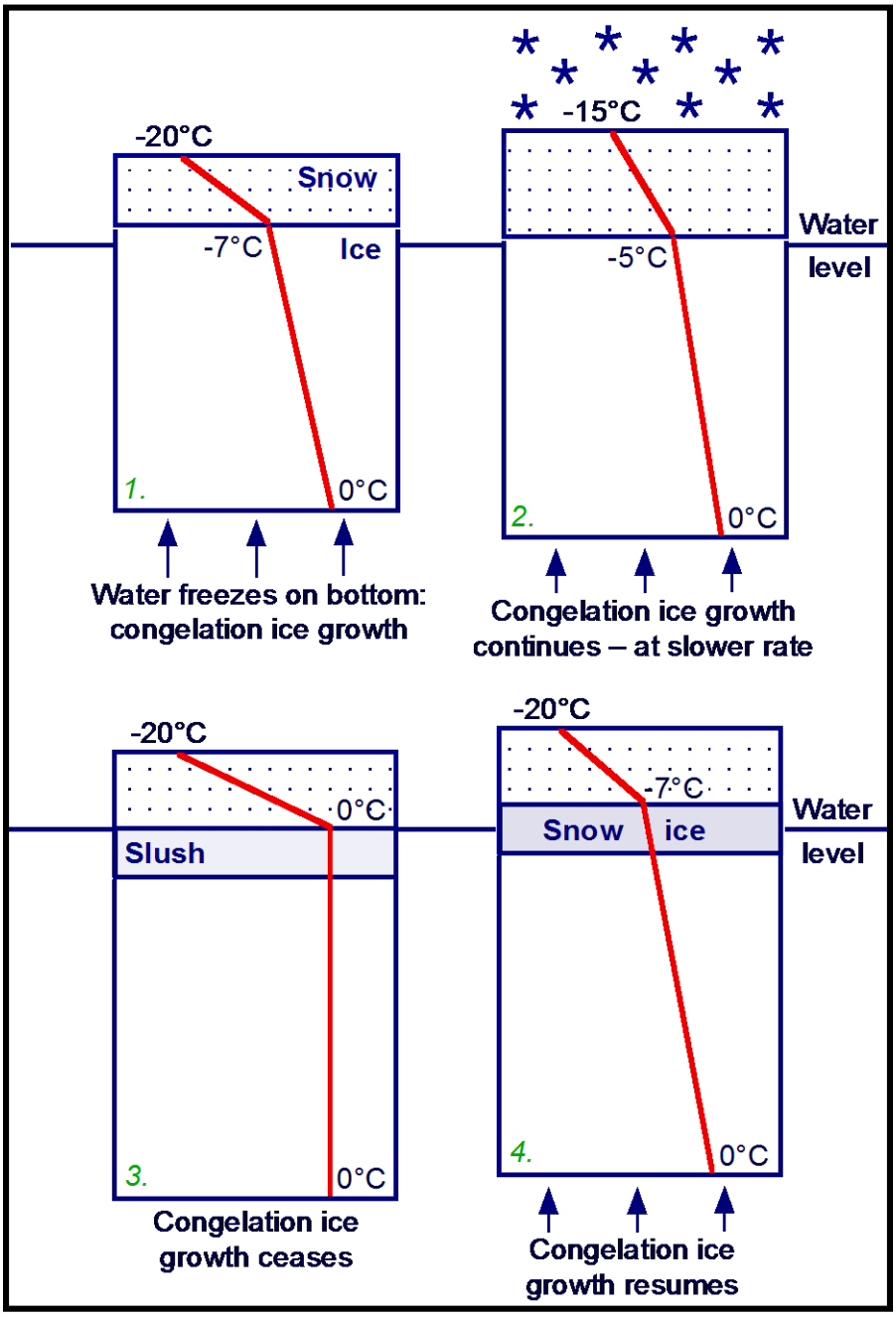

Figure 2. 1 Schematic showing stages in the formation of congelation (black) ice and snow ice. Figure courtesy of M. Jeffries and K. Morris. In (1) and (2), the congelation ice growth rate is shown in the absence and presence of snow, while in (3) the formation of slush is shown when the congelation ice growth ceases. In (4) the resumption of congelation ice growth and the formation of snow-ice are shown.

Other than temperature, there are other climate and non-climate-related drivers affecting ice phenology during the freeze-up, break-up, and ice season periods, including precipitation, presence or absence of clouds, inflow of water from rivers, the depth and the shape of the lake, and the latitude and elevation of the lake (Hoekstra, 2018; Murfitt, 2018). Meanwhile, the presence of snow cover on the ice surface is one of the key factors to consider in GNSS-IR experiments at mid-latitudes because slush and wet snow are contributing layers affecting GNSS multipath signals. The effect of snow cover is expected to be minimal in Arctic and sub-Arctic regions where winter temperatures are colder and snow accumulation on ice, with a few exceptions, tends to be less important.

2.1.2. Lake ice remote sensing

As a sensitive indicator of climate change the topic of remote sensing of lake ice has gained significant interest in recent years (Duguay et al., 2015). Optical remote sensing data (e.g. MODIS and LANDSAT series products) have been used to monitor variations and recent trends in ice phenology (Brown & Duguay, 2012; Murfitt & Brown, 2017). Radar remote sensing, with its all-weather and day-night acquisition capabilities, has also been used to map ice and open water areas and ice phenology (Duguay et al., 2015). Based on radar returns which are affected by lake ice properties and open water conditions (calm or windy), ice dates during freeze-up and break-up periods as well as ice cover duration can be determined (Murfitt , 2018).

In addition to the mapping and monitoring of open water and ice-covered areas and the determination of ice dates, satellite remote sensing has been used to estimate lake ice thickness. For example, Kang et al. (2014) developed an algorithm for retrieving ice thickness on a daily and monthly basis using the Advanced Microwave Scanning Radiometer-Earth Observing System (AMSR-E) based on the temporal evolution of brightness temperature at the 18.7 GHz frequency

(V-polarization). Compared to limited field measurements and numerical simulations with the Canadian Lake Ice Model (CLIMo) from Great Bear Lake (GBL) and Great Slave Lake (GSL) in the Northwest Territories, the algorithm was shown to perform well with an RMSE of 19 cm. In addition, lake ice surface temperature data obtained from Moderate Resolution Imaging Spectroradiometer (MODIS) was used to estimate lake ice thickness (Kheyrollah Pour et al., 2017). The RMSE of this approach, in comparison with CLIMo simulations from GSL and Baker Lake (Nunavut), was determined to be 17 cm; however this approach was limited to ice columns not thicker than 1.7 m. Furthermore, Beckers et al. (2017) used data from the CryoSat-2 radar altimeter to estimate ice thickness also from GBL and GSL with an RMSE of better than 33 cm compared to in-situ measurements. Aside from satellite remote sensing, a study by Gunn et al. (2015) on Malcolm Ramsay Lake near Churchill, Manitoba, derived freshwater ice thickness using ground-based X- and Ku-band scatterometers with a strong agreement (coefficients of determination up to 0.96 and RMSE in the order of 7 cm) with in-situ observations and CLIMo simulations.

Besides remote sensing, the growth of ice can be simulated using temperature-based models linking accumulated freezing/thawing degree days with increasing/decreasing ice thickness, known as Stefan's and Bilello's equations (Bilello, 1980; Stefan, 1890), in addition to more complex 1-dimensional thermodynamic ice models such as CLIMo (Duguay et al., 2003). The coefficients for these simpler models have been tuned and determined for temperate lake ice covers resulting in ice thickness estimations with a correlation of ~0.9 and RMSE of 2.3 and 2.1 cm during ice growth and ice decay, respectively (Murfitt et al., 2018). This study has tuned Stefan's coefficient for MacDonald Lake, where the mid-latitude experiment of this thesis was conducted on its shore.

2.2. GPS

The Global Positioning System (GPS), as the first GNSS system, was developed by the Department of Defense (DoD) of the U.S. and declared as an operational system in 1995. Its method of positioning is called “trilateration” in which the position of a receiver is estimated by measuring its distance to, at least, four satellites with known positions. The distance between a satellite and a receiver is called “pseudo-range” and is calculated by estimating the travel time between the transmitter (satellite) and the receiver. The original constellation designed for GPS contained 24 medium Earth orbit (MEO) satellites located at a distance of 20,200 km from the Earth, in order to provide proper visibility to the sufficient number of satellites for solving the three-dimensional positioning for a receiver at any location on the Earth. Nowadays, with a constellation of 32, GPS satellites provide users with a higher precision in positioning, and it is highly probable to see eight or more GPS satellites at any one time. Before describing the basics of GNSS-IR, an overview of the basics of GPS, and then, multipath GPS signals is provided.

2.2.1. The principle of GPS

GPS signals carry “navigation data messages” at the rate of 50 bit-per-second (bps), which contain necessary information for positioning. Some of these parameters are clock correction, ephemerids and almanac (versions of satellites’ positions and velocity vectors), atmospheric corrections, and satellites’ quality indices. These data blocks are controlled by a set of ground control stations (control segment) and uploaded to satellites. Correlating the GPS signal with a replica of the GPS “ranging-code” sequence (called pseudo-random code, PRN), a GPS receiver is able to discern among different satellites’ signals and estimate the pseudo-range based on the correlation peak.

Each GPS satellite transmits signals using three frequencies at L-band known as L1 (1.57 GHz), L2 (1.22 GHz), and L5 (1.17 GHz). Each GPS signal is comprised of a carrier sinusoidal signal, a ranging code, and the navigation data message. There are three different ranging codes designed for different purposes, including coarse/acquisition (C/A) code, precise (P) code, and military code (M). Among these codes, C/A code is open access for standard users and carried on L1; however, a civil code like the C/A code has been recently added to L2 (called L2C). Since the focus of this thesis is not GPS positioning, readers who are interested in finding more about GPS are encouraged to go through other comprehensive resources for more details (Hofmann-Wellenhof et al., 2007; Samama, 2008; Xu & Xu, 2016).

Except for GPS, the GLONASS (in Russian: Global'naya Navigasionnaya Sputnikovaya Sistema) is another operational GNSS constellation with 24 operational satellites, which are visible worldwide. GNSS receivers are currently benefiting from GPS, GLONASS, Galileo (initiated by the European Space Agency), and BeiDou (Developed by the Chinese government) at the same time, and the accuracy of positioning is expected to become much better due to the improved combination of these systems.

While most commercial geodetic GNSS receivers, as the main observation tools used in this thesis, are able to calculate, present, and store their real-time positions; other intermediate measurements are stored in their raw files as well. These raw files can be converted into a common format file that is called RINEX (Receiver Independent Exchange Format) consisting of parameters such as pseudo-range, phase observations, Doppler frequencies, and the signal-to-noise ratio (SNR) of received signals, as well as information on the timely locations of satellites. Figure 2.2 shows an example of an observation RINEX file (Version 2.1), including the header and some of the observations recorded in the very first epoch of time. The header includes the approximate

position of the receiver, the time of the first and the last observations in this file, and all types of observations. Afterwards, the observations list is presented for the date of January 1, 2020, at the UTC time of 16^h 46’ 54” for 24 satellites including GPS (G), GLONASS (R) and Galileo (E). The last (right) column of observations represented in Figure 2.2 shows the SNR values recorded by the antenna for each observation.

```
     2.11           OBSERVATION DATA    M (MIXED)           RINEX VERSION / TYPE
CONVBIN 2.4.3 Emlid                     20200102 164916 UTC PGM / RUN BY / DATE
log: raw_202001011649                                       COMMENT
format: u-blox                                              COMMENT
                                                            MARKER NAME
                                                            MARKER NUMBER
                                                            OBSERVER / AGENCY
                                                            REC # / TYPE / VERS
                                                            ANT # / TYPE
   891065.5657 -4410600.3259  4505646.5239                  APPROX POSITION XYZ
        0.0000        0.0000        0.0000                  ANTENNA: DELTA H/E/N
     1     1                                                WAVELENGTH FACT L1/2
     8    C1    L1    D1    S1    C2    L2    D2    S2      # / TYPES OF OBSERV
  2020     1     1    16    46   53.9960000     GPS         TIME OF FIRST OBS
  2020     1     2    16    46   49.9900000     GPS         TIME OF LAST OBS
                                                            END OF HEADER
 20  1  1 16 46 53.9960000  0 24E24E25G32G25E15E 5G31G24G10G20G14G11
                              R14E 3R 4R 3G12G 1R 5R13R20G18R15R21
  22873727.568 1 120202229.242 1     -1561.117          43.000

  23538669.215 1 123696534.350 1      1277.509          45.000

  19316807.660 1 101510513.52811       273.791          52.000

  21396443.117 1 112439085.39511      2319.172          41.000

  25796658.759 9                     -3007.754          25.000

  24616498.456 1 129360542.536 1     -2241.821          42.000

  21435516.249 2 112644406.96511      3048.920          37.000

  22613396.261 1 118834239.41911     -3787.299          42.000
```

Figure 2. 2 Example of RINEX file, including the header and the beginning part of the observations.

2.2.2. Multipath signals

In geodetic positioning, the term multipath is referred to reflections from the surrounding area and objects close to the GNSS antenna deployed in the field and is considered as an error that results in a poor positioning quality. Therefore, geodesists are using some techniques to avoid receiving multipath signals. For instance, GNSS signals are designed with right-handed circular polarization (RHCP), while reflected GNSS signals are mostly left-handed circular polarized (LHCP). Thus, geodetic GNSS antennas are designed to receive only RHCP signals and refrain from receiving LHCP multiple signals; however, amounts of RHCP signals can be found in reflected signals, which can be reduced by means of mathematical models. Researchers in satellite geodesy have modelled the multipath interferences with the direct signals to remove the multipath effects on positioning (Amiri-Simkooei, 2005; Byun et al., 2002).

In contrast, multipath signals are the seminal observation in reflectometry, and should be discerned from direct or composite GNSS signals. The voltage of the receiving signal SNR_c is the sum of the voltage values of direct SNR_d and reflected SNR_r signals, which are described as follows (Georgiadou & Kleusberg, 1988):

$$SNR_c = SNR_d + SNR_r \tag{1}$$

$$SNR_d = A_d \cos\varphi \tag{2}$$

$$SNR_r = \beta A_d \cos(\varphi + \psi) \tag{3}$$

where A_d denotes the direct signals voltage amplitude, β is between 0 and 1 showing the reduction in the voltage amplitude, the φ is the signal phase, and ψ is a phase shift attributed to the multipath. The phase shift has been geometrically shown to be associated with the vertical distance of the receiver from the reflective surface (H), in the case where the reflective surface is assumed as a

planar horizontal surface (Bishop et al., 1985; Georgiadou & Kleusberg, 1988; Nievinski & Larson, 2014):

$$\psi = \frac{2H}{\lambda} 2\pi \sin e \tag{4}$$

where λ is the wavelength of the signal (19 cm for the GPS L1) and e denotes the elevation angle of the transmitting vehicle (i.e. GPS satellite). Substituting (4) in (3), the voltage of the reflected signal can be written as follows:

$$SNR_r = A_r \cos(\frac{4\pi H}{\lambda} E + \varphi) \tag{5}$$

where A_r is the reduced amplitude for reflected signal and E is a substitution for the sine of the satellite elevation angle. Subtracting a low-order polynomial from the voltage of the receiving signal (SNR_c), as demonstrated in previous studies (Larson et al., 2009a), one can obtain the SNR of the multipath signal from the combined, interfered signal received to the antenna. As an example, the SNR values given in the sample RINEX file, shown earlier in Figure 2.2, are extracted out, and after removing a second-order polynomial, the variation of SNR_r against E is plotted as shown in Figure 2.3. As formulated in (5), the receiver height (H) can be derived from the "frequency" of the voltage of the reflected signal (SNR_r); therefore, the SNR time series should be processed to retrieve predominant frequencies. It is expanded upon in section 2.4.

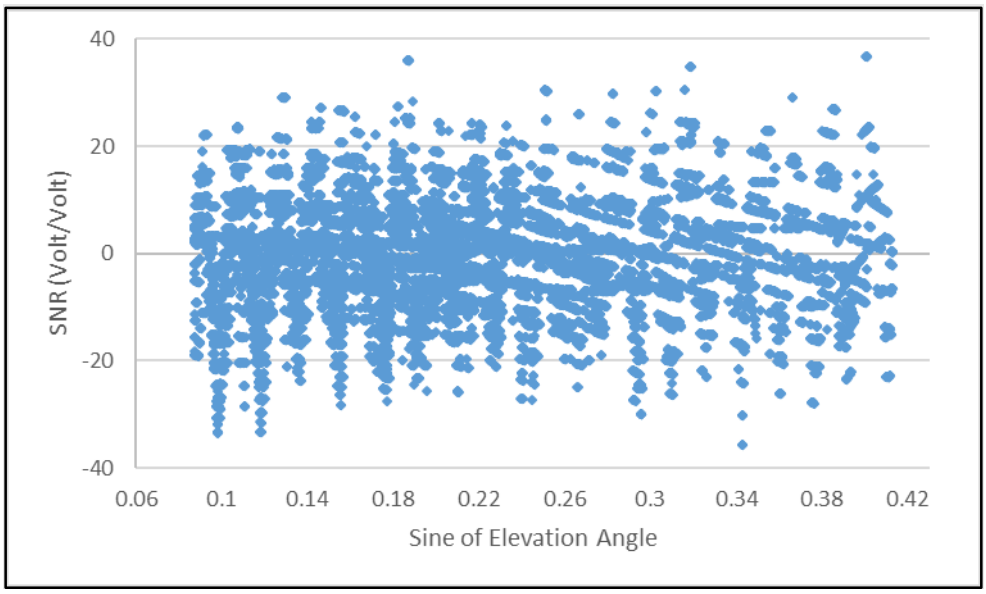

Figure 2.3. The oscillation of L1 SNR data against the sine of the elevation angle of satellites.

2.3. GNSS Reflectometry

The use of reflected GNSS signals as a remote sensing tool was first proposed in 1993 for ocean altimetry and known as Passive Reflectometry and Interferometry System (PARIS) (Martin-Neira, 1993). Afterwards many other experiments begin utilizing reflected GNSS signals for sea ice detection (Komjathy et al., 2000) and wind speed measurements (Garrison et al., 2002; Rius et al., 2002). As the first reflected GNSS signals were detected from space, UK-DMC-1 satellite was launched in 2003 for ocean sensing and ice detection (Gleason, 2006). Following the UK-DMC-1 mission, TechDemoSat-1 was launched as the second GNSS reflectometry satellite in 2014 with advancements in instrumentation to help researchers in ocean wind measurements (Foti et al., 2015), soil moisture retrieval (Chew et al., 2016), and sea ice phase altimetry with root-mean-square-difference (RMSD) of 5 cm (Li et al., 2017). Currently, CYGNSS is the only operational GNSS-R system launched by National Aeronautics and Space Administration (NASA) and

consists of 8 Low Earth Orbit (LEO) micro-satellites. CYGNSS footprints cover low-latitude regions (38^{o}N - 38^{o}S) and the main purpose of the mission is measuring ocean wind speed in the tropical cyclone inner core (Clarizia et al., 2015). That said, studies have been recently conducted to examine the ability of CYGNSS for soil moisture retrieval (Chew & Small, 2018) as well as for ocean and lake water height retrieval (altimetry) (Li et al., 2019; Mashburn, 2019). The fundamental design for the above-mentioned GNSS-R missions is based on using two GNSS antennas to receive direct and reflected signals separately. These multi-receiver systems consist of one up-looking RHCP antenna to receive direct line-of-sight signals and one nadir-looking LHCP antenna to receive the reflected GNSS signals. These systems are commonly called GNSS-R in the literature (Zavorotny et al., 2014).

In addition to GNSS-R space missions, the reflectometry technique has been employed extensively in ground-based experiments by using single geodetic GNSS receivers. The term "interferometry" is used for this type of measurement because both direct and reflected signals are received by a single receiver and the signals cause interference on each other. Soil moisture content (SMC) and the variability in SMC were the first values derived by means of GNSS-IR (Larson et al., 2008; Larson et al., 2009b). Estimating the amplitude and the phase of multipath SNR as in Equation 6, researchers have modeled variability in SMC (Chew et al., 2013; Zhang et al., 2017). In addition to the amplitude and phase shift in SNR, researchers have extracted the frequency of SNR time series to retrieve the GNSS antenna height from the reflective surface and, by implication, the variations in surface elevation. Attaining the antenna height from the reflective surface, researchers have been able to track variations in snow depth (Larson, 2016), vegetation height (Zhang et al., 2017), and vertical movements of the ground in permafrost regions (Liu & Larson, 2018).

In general, the configuration of GNSS-IR is visualized as a "bi-static (multi-static) radar" system since the transmitter(s) and the receiver are not placed at the same location. In other words, signals are not reflected back in the same direction towards the transmitter (GNSS satellites), but reflected in the opposite angle towards the receiver. Figure 2.4 shows the basics of GNSS-IR as a bistatic radar system; however, the radar equation is not among the topic of this study; more details on the theory of radar can be found in the relevant literature (Ulaby et al., 1981).

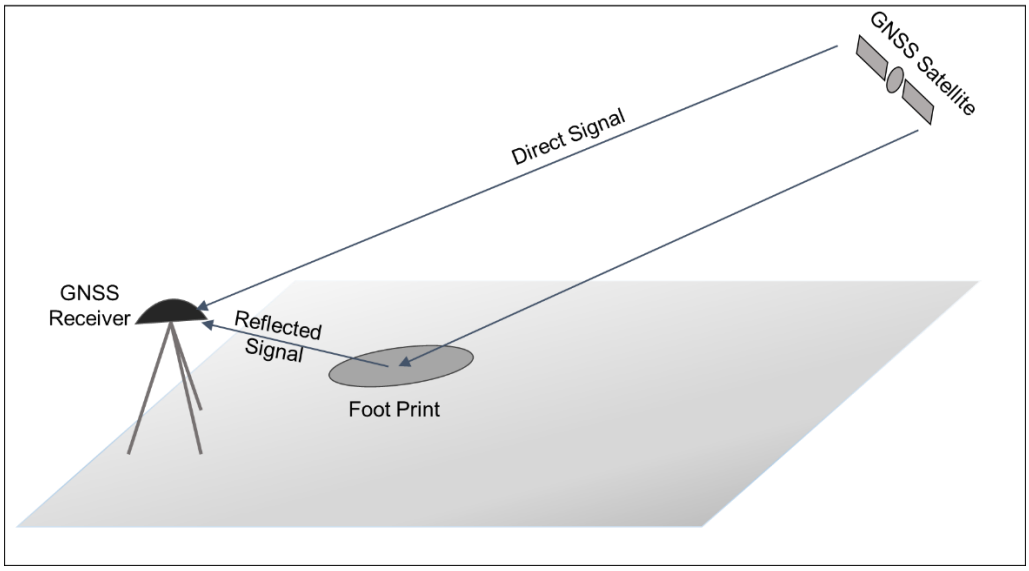

Figure 2.4. Basics of GNSS-IR. Both direct and reflected GNSS signals are received by a single GNSS receiver.

By assuming a stationary location for the receiver, the size, shape and the direction of the footprint shown in Figure 2.4 varies as the azimuth and elevation angle of the GNSS satellite also vary over the time. Considering all visible satellites, and their movement over time, a large number of ellipse-shaped footprints are generated around the receiver such that their long and short axis (a, b) and their distance from the antenna (R) can be geometrically determined as follows (Vey et al., 2016):

$$b = \sqrt{\frac{\lambda H}{E} + \left(\frac{\lambda}{2E}\right)^2}\,, a = \frac{b}{E}\,, R = (H + \frac{\lambda}{2E}) \tan e \qquad (7)$$

However, in GNSS-IR experiments restricted to GNSS satellites with elevation angles in the range of 5-25^{o}, because in GNSS-IR only RHCP reflections are desirable at this range of elevation angle, RHCP signals can be easily found (Zhou et al., 2019). Finally, having several footprints (or SNR) generated by reflected signals from multiple satellites with known elevation angles, time series of SNR variations can be extracted as formulated in (6) and as shown in Figure 2.3. The desirable parameter in (6) is the frequency of the SNR fluctuation ($\frac{4\pi H}{\lambda}E$) to extract the only unknown parameter, which is the height of the antenna (H). The reference point for any GNSS antenna is called *antenna phase centre (APC)* at which the GNSS signals are received. The APC is not necessarily the geometric centre of the antenna and needs to be determined or calibrated by manufacturers and specialists. In this thesis, the word "antenna height" refers to the height of the antenna phase centre.

2.3.1. GNSS-IR for the retrieval of lake ice thickness

It is known from the physics of remote sensing that microwave signals at L-band largely penetrate through snowpack and ice cover under dry conditions, and reflected from the underlying water surface (Engram et al., 2013). Figure 2.5 shows the schematic diagram of the GNSS reflection from lake ice and snow-covered lake ice with different scenarios of material conditions that may be observed in the field during the ice growth period.

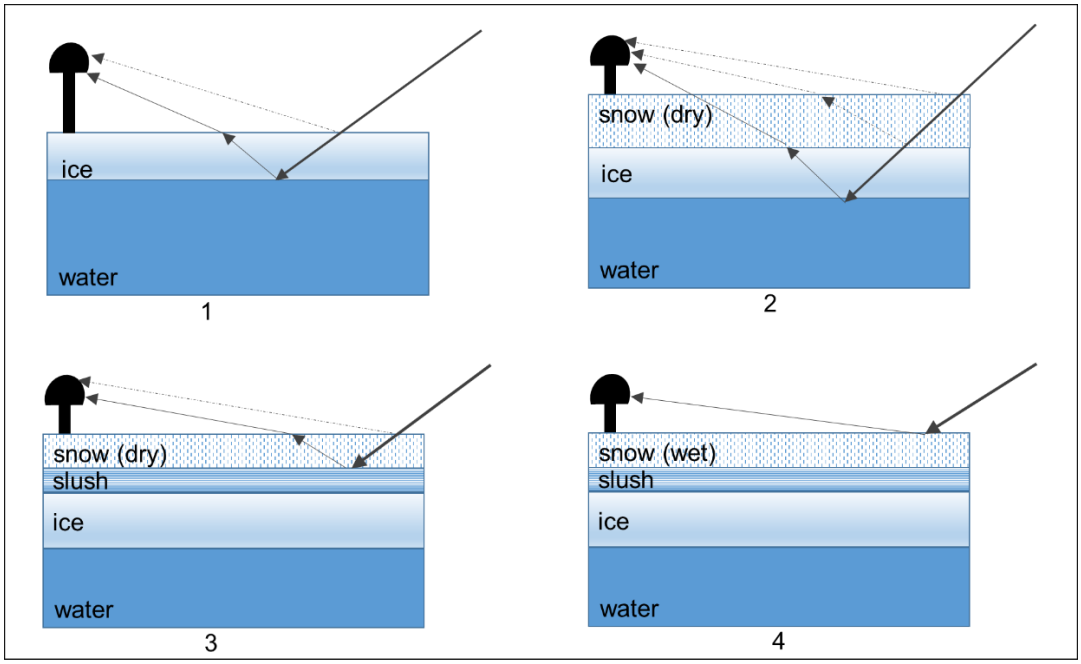

Figure 2.5. Schematic diagram of GNSS reflection from lake ice for four different scenarios. The thick arrow in each scenario represents the transmitted signal from the satellite. Thin solid arrows represent the most prominent reflection, and dashed arrows represent less-prominent reflections.

The first scenario in Figure 2.5 illustrates a case where the only layer above the water is either black (clear/congelation) ice or grey/white ice, which is called the total ice column. The GNSS signal easily penetrates through the ice and is reflected back as it reaches water beneath the ice column. Thus, the ice-water interface acts as the reflective surface, and knowing the height of the receiver, one can determine the ice thickness by deriving H from equation (6). This scenario is mostly encountered on Arctic and sub-Arctic lakes where the ice surface can be snow-free early in the ice season and due to the redistribution of snow by winds. The second scenario shows the reflection in the presence of a dry snowpack above the ice surface. Similar to the first scenario, the dominant reflection comes from the ice-water interface; the dielectric contrast between air, dry snow, and ice is so low that no dominant reflection is detected from these interfaces. However, less dominant reflection may be expected from air-snow and snow-ice interface. Researchers have

theoretically corroborated some L-band reflection from the top of the snowpack (Yueh et al., 2017).

In the third scenario, the reflection pattern in the presence of a layer of slush (see Chapter 2, section 2.1.1 for description), is different from the first two scenarios. Here the slush layer acts as water with a high dielectric constant. Hence, the dominant reflection comes from the top of the wet slush layer in this scenario and from the surface of the wet (melting) snowpack in the fourth scenario. In these last two scenarios, a very weak reflection, if any, is expected to be received from the layers beneath. Nonetheless, the penetration depth into wet layers such as wet snow and slush are highly dependent on the density of these layers, meaning that layers beneath may slightly contribute to the total reflection received by the antenna.

The two last scenarios are very likely to occur on mid-latitude lakes, such as MacDonald Lake, compared to higher-latitude ones, because of the warmer and fluctuating air temperatures experienced in these regions (hovering below and above 0^{o}C). Figure 2.6 shows the average, maximum, and minimum daily air temperature fluctuations at MacDonald Lake in winter 2020, which were recorded from a weather station installed on the southern shore of the lake. As can be seen, the mean temperature is very unstable and reaches above 0^{o}C for several days. Therefore, melt and, by implication, wet layers are expected, which can hinder GNSS signals from reaching the ice-water interface. As well, the refreezing of wet snow into ice crusts or ice lenses, and slush into snow ice may affect the GNSS reflected signals but the impact of this (importance and magnitude) is currently unknown. Examination of such impacts is beyond the scope of this thesis but is certainly a topic that would merit investigation through detailed field measurements and microwave radiative transfer model simulations.

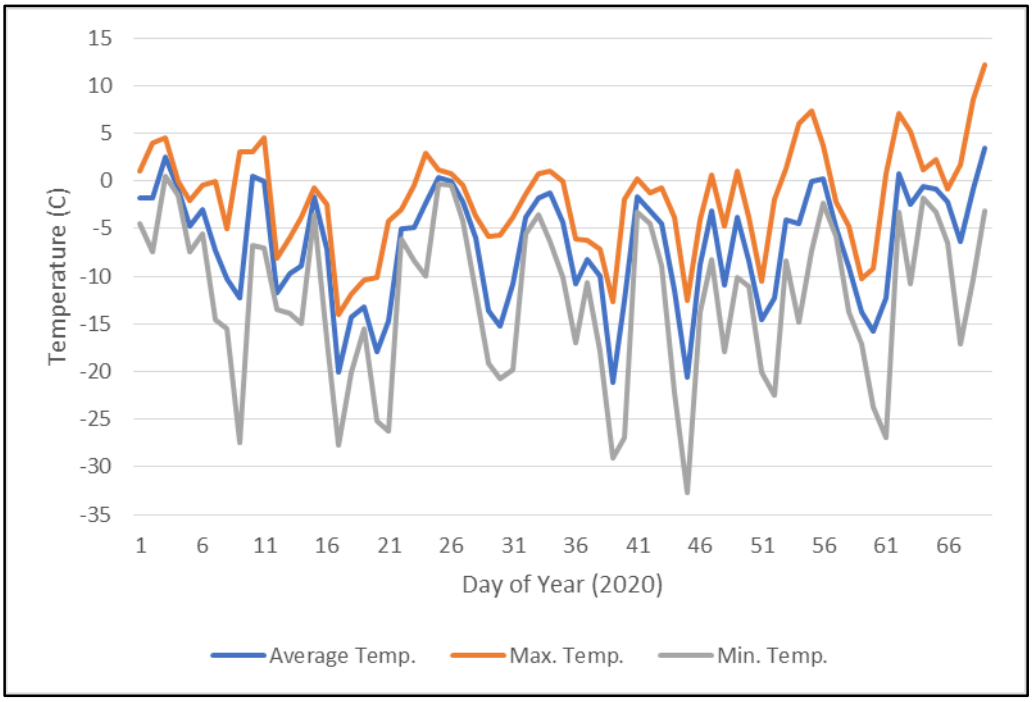

Figure 2.6. Average, maximum, and minimum daily air temperature fluctuations at the MacDonald Lake during winter 2020.

2.3.2. GNSS-IR for lake ice detection

By changing the lake phase from water to ice, the coherency of the reflection will drastically increase. Based on this change in the reflection coherency, researchers have been able to discriminate sea ice from open water using data from GNSS-R missions such as TDS-1 and CYGNSS (Fabra et al., 2011). With freezing, the roughness of the water surface drops, which boosts the power of the coherent reflection. In contrast, when ice disappears in springtime, the coherency of the reflection is hampered. The GNSS-IR technique examined in this thesis, as well as with GNSS-R missions, can utilize coherence to provide users with freeze-up/break-up timings. Figure 2.7 presents an example of voltage frequency peaks obtained during the freeze-up period of late fall 2019 at MacDonald Lake. We show data from this lake here, and expanded upon in

Chapter 4, since no previous studies have explored the use of GNSS-R or GNSS-IR for the detection of ice-on and ice-off dates.

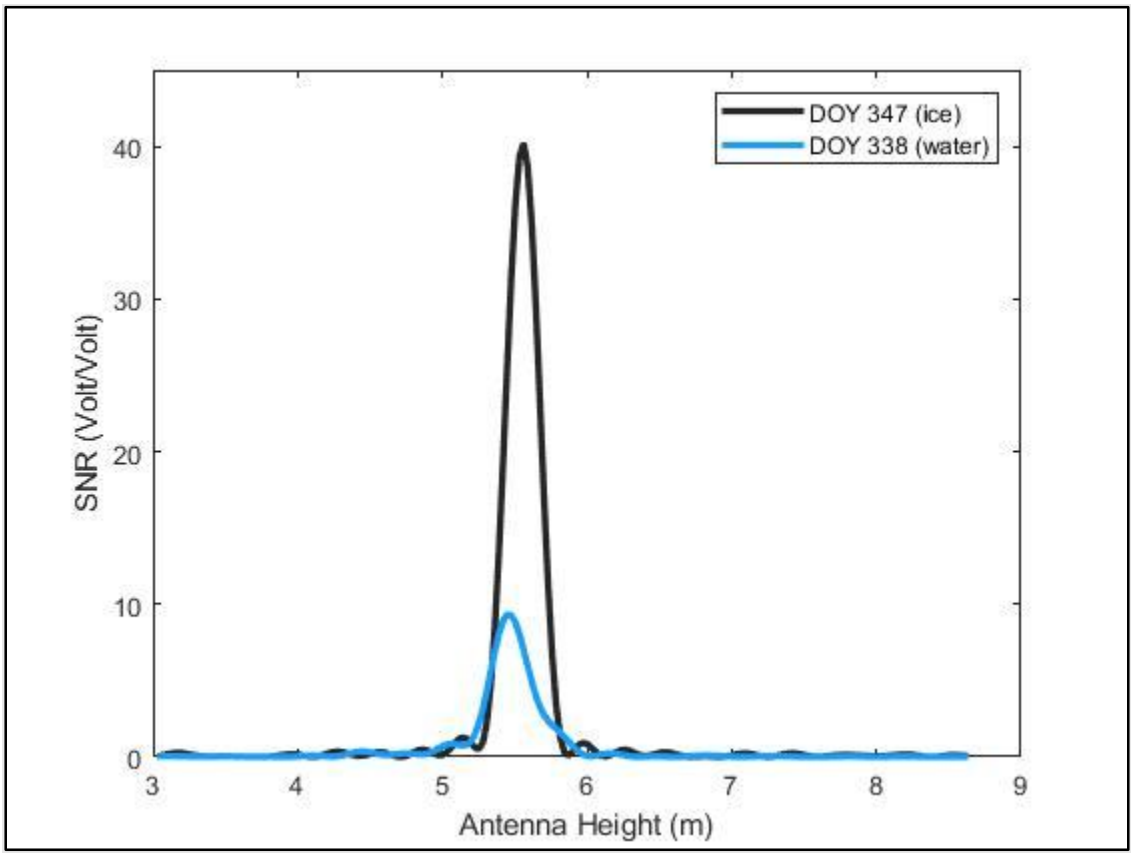

Figure 2.7. SNR frequency peaks obtained for DOY 338 (open water) and DOY 347 (ice cover).

As shown in Figure 2.7, the frequency obtained for the SNR of the signal reflected off the thin, recently formed, ice surface (DOY 347) is much larger than that obtained under open water conditions (DOY 338). The power of the black peak is ~4 times greater than that of the blue one, which illustrates the power of the reflection from the ice-covered surface compared to that of the water surface. Using this feature, the timing of freeze-up and break-up can be determined by means of GNSS-IR.

2.4. SNR Time Series Analysis

As mentioned in previous sections, the unknown parameter in the SNR equation that we are interested in is the frequency of the SNR time series, which leads us to the extraction of the antenna height from the reflective surface(s). As discussed in the section 2.3.1, there may be multiple layers, at different depths, contributing to the total reflection received by the antenna; therefore, each reflective layer adds a specific frequency to the SNR time series. The aim of this thesis is retrieving as many significant frequencies as possible from the SNR time series to obtain the thickness of each contributing layer.

The alternative terminology for "frequency" in the literature is "period", which is frequently used by GNSS-IR researchers. Similarly, methods used to obtain the period are generally called "periodogram". The most known periodogram in science is "Fourier", which transforms data from the spatial domain into the frequency domain as to retrieve frequencies laid in the data. However, in this thesis, the Least-Squares Harmonic Estimation (LS-HE) method is preferred rather than Fourier since the latter is limited to evenly spaced data and return only integer frequencies (Amiri-Simkooei, 2007), while in this research, the data are not necessarily evenly spaced and non-integer frequencies are required as well. Furthermore, this study calls for the extraction of less-dominant frequencies to represent all contributing layers. By applying the LS-HE method, one is able to omit the most dominant frequency as a functional model and retrieve the next dominant frequency. This iterative process can be run for three or four times to find a set of frequencies of SNR time series. Many applications of the LS-HE method can be found in literature, especially in geodesy and GNSS analyses (Amiri-Simkooei & Parvazi, 2017; Amiri-Simkooei & Asgari, 2012; Asgari & Harmel, 2001).

2.4.1. Least-square harmonic estimation

Any given time series, such as SNR time defined as $S^T = [S_1, S_2, \dots, S_n]$, shown in equation (6), can be rewritten as the sum of a linear trend and *p* individual trigonometric terms as follows:

$$S = (S_0 + AE) + \sum_{i=1}^{p} a_i \cos(\omega_i E) + b_i \sin(\omega_i E) \tag{8}$$

where S_0 and A are the initial intercept and linear slope, respectively, and a_i and b_i are the unknown real numbers representing the coefficients of the trigonometric terms. The frequency, ω_i, which is equal to $\frac{4\pi H_i}{\lambda}$ as shown in equation (6) is the desired parameter that should be identified through the LS-HE method. In matrix notation, equation (8) may be rewritten as follows:

$$S = (S_0 + AE) + \sum_{i=1}^{p} A_i x_i \tag{9}$$

such that

$$A_i = \begin{bmatrix} \cos(\omega_i E_1) & \sin(\omega_i E_1) \\ \cos(\omega_i E_2) & \sin(\omega_i E_2) \\ \vdots & \vdots \\ \cos(\omega_i E_n) & \sin(\omega_i E_n) \end{bmatrix}; \ and \ x_i = \begin{bmatrix} a_i \\ b_i \end{bmatrix} \tag{10}$$

In other words, E are the observations, S is the equations system, and ω_i are the frequencies we need to estimate to retrieve the antenna height (H_i). The following maximization approach is applied to identify the frequency ω_i (Amiri- Simkooei et al., 2007):

$$\omega_i = arg \max_{\omega_j} P(\omega_j) \tag{11}$$

with

$$P(\omega_j) = P_A^{\perp} S A_j (A_j^T P_A^{\perp} A_j)^{-1} P_A^{\perp} S \tag{12}$$

$$where \quad P_A^{\perp} = I - A_j (A_j^T A_j)^{-1} A_j^T$$

The design matrix A_j is structurally the same as A_i that ω_i is substituted with ω_i, and among different design matrices, the one maximizing $P(\omega_j)$ is set to be A_i. Since analytical methods for the maximization of equation (11) may be complicated, one can perform a numerical evaluation, in which a plot of $P(\omega_j)$ against discrete values of ω_j is used to obtain the contribution of each frequencies in the construction of SNR original time series (S), and find the maximum frequency. Detecting the ω_1 as the dominant frequency, one should add the sine and cosine terms of ($\omega_1 E_1$) to the initial design matrix in equation (10) and rebuild a new design matrix to detect the next dominant frequency. Although statistical tests are commonly used to validate the significance of a frequency in geodesy studies, in the current research one can examine the relevance of a frequency by observing the shape of the spectral power (Figures 2.8 and 2.9), as we know that the number of significant frequencies is not too large. In this thesis, the ratio of peak to background noise is considered as the criterion for the significance of frequencies.

2.4.2. LS-HE for antenna height retrieval

Identifying frequencies ω_i in SNR time series, one can retrieve the height of the antenna above multiple reflective layers as follows:

$$H_i = \frac{\omega_i \lambda}{4\pi} \tag{13}$$

Based on the lake condition (scenarios shown in Figure 2.5), the number of significant frequencies varies from 1 to 4, and one can ignore non-significant frequencies since their spectral power plot do not contain a sharp unique peak. For instance, the first four antenna-heights retrieved from the LS-HE method for the DOY 324 of 2019 is shown in Figure 2.8, which shows that the

only significant layer is the first one since the lake is not yet frozen at this time, and the only existing layer is the water surface. Figure 2.9 is another example of height retrieval for DOY 64 of 2020, in which four significant antenna heights are obtained, which are hypothesized to represent four existing layers, i.e., the top of the snowpack, snow-ice interface, slush layer, and ice-water interface.

In this study, the LS-HE method is applied to daily SNR time series to obtain the antenna height from existing reflective layers, if applicable, based on the conditions. Next, the evolution and variation of the existing layers is derived from daily antenna heights and compared with in-situ measurements and supplementary data. The next two chapters present the application of this approach to high-latitude (Chapter 3) and mid-latitude (Chapter 4) lake sites that are affected by contrasting winter conditions.

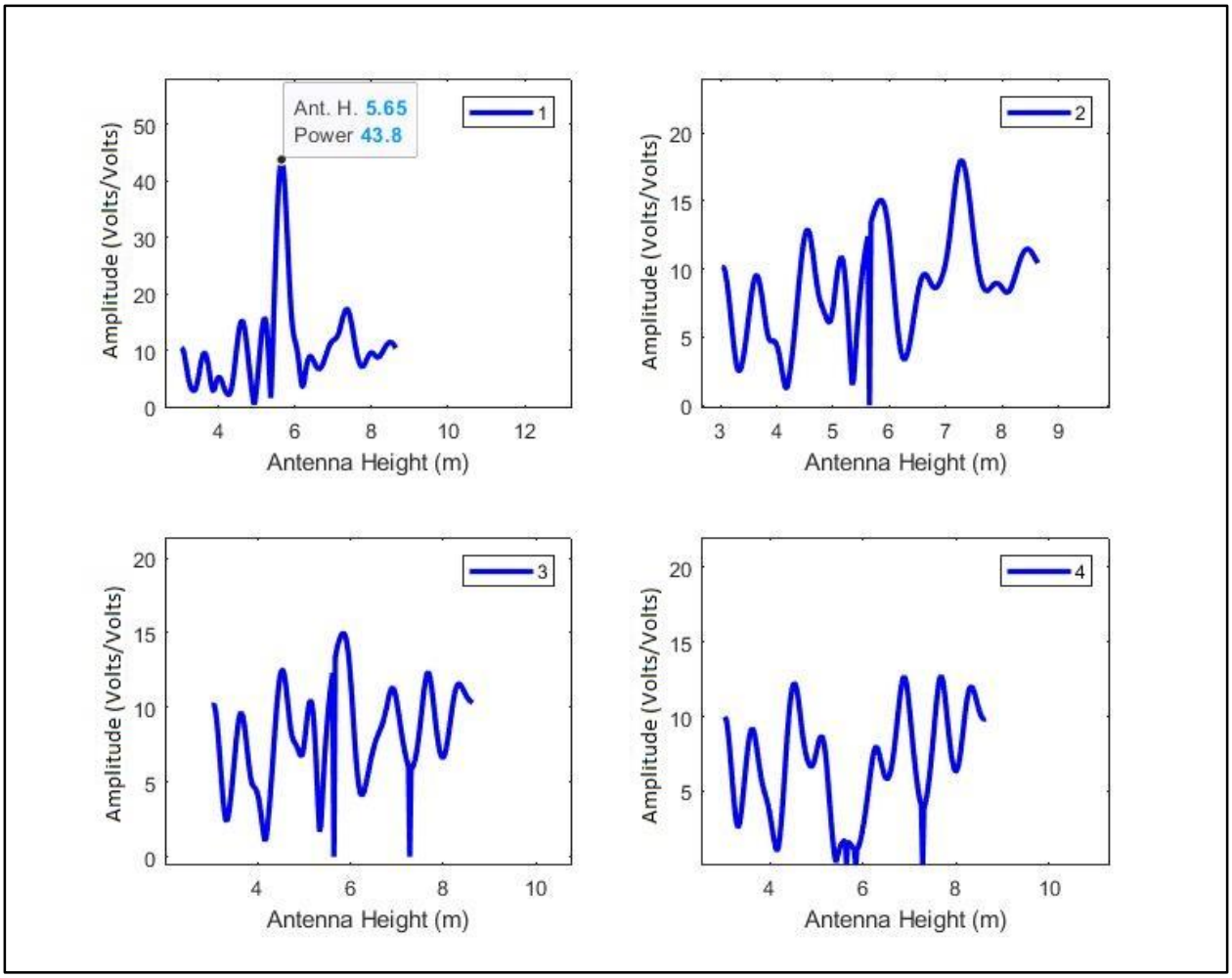

Figure 2.8. The spectrum of the first four harmonics of the SNR time series for DOY 324 of 2019. The dominant peak in the top left figure (first harmonic) represents for the antenna height above the only existing reflective layer (water). Other harmonics return no significant peak because there is no more reflective layer.

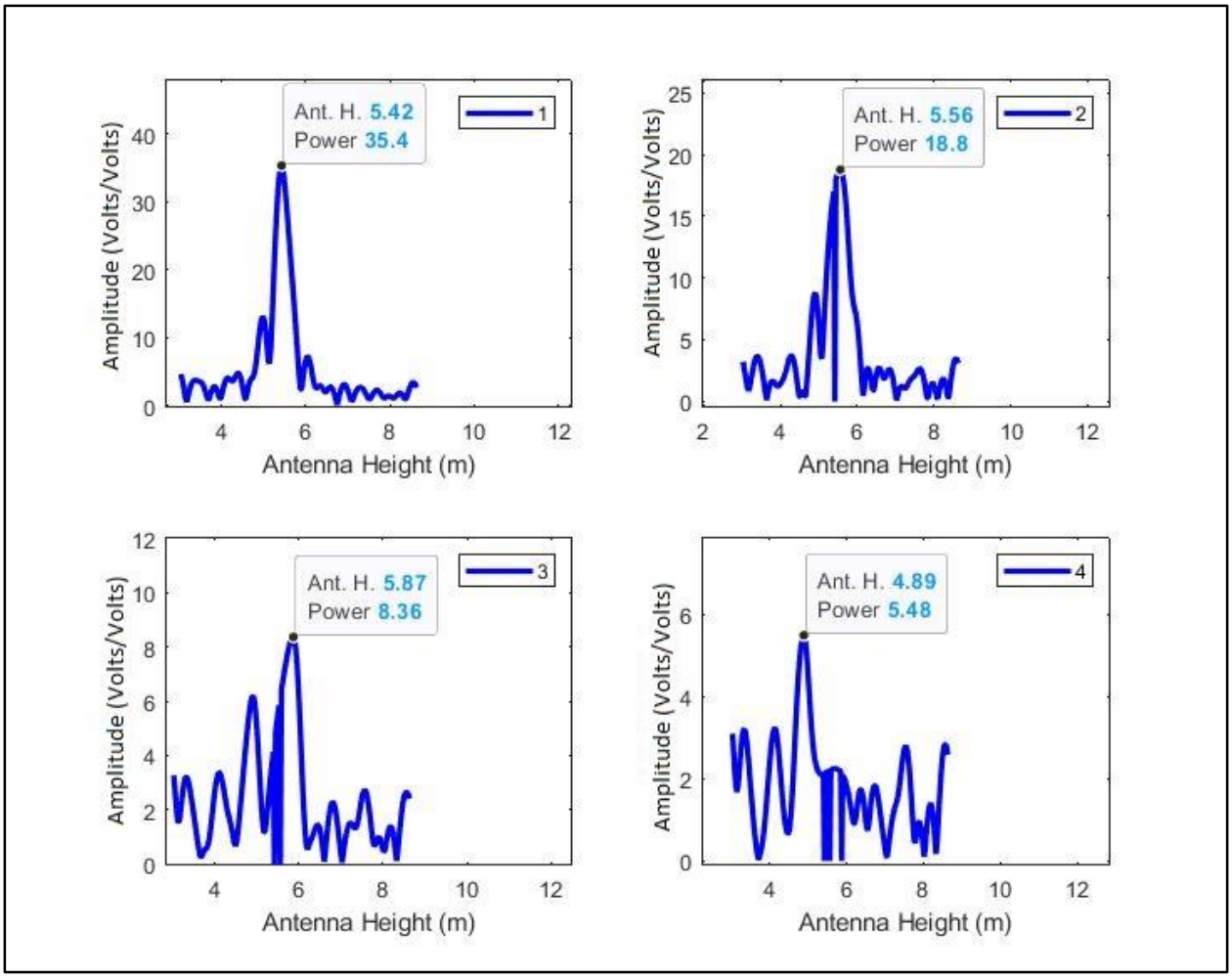

Figure 2.9. The spectrum of the first four harmonies of the SNR time series for DOY 64 of 2020. In this example, four significant peaks are determined representing for the antenna heights above four different overlaying layers.

Chapter 3 – Application of GNSS Interferometric Reflectometry for the Estimation of Lake Ice Thickness

This chapter includes a paper published in the Journal of *Remote Sensing* on 23 August 2020.

Journal version:

Ghiasi, Y., Duguay, C. R., Murfitt, J., van der Sanden, J. J., Thompson, A., Drouin, H., Prévost, C. (2020). Application of GNSS Interferometric Reflectometry for the Estimation of Lake Ice Thickness. *Remote Sensing, 12,* 2721, doi:10.3390/rs12172721. [2]

3.1. Abstract

Lake ice thickness is a sensitive indicator of climate change largely through its dependency on near-surface air temperature and on-ice snow mass (depth and density). Monitoring of the seasonal variations and trends in ice thickness is also important for the operation of winter ice roads that northern communities rely on for the movement of goods as well as for cultural and leisure activities (e.g. snowmobiling). Therefore, consistent measurements of ice thickness over lakes is important; however, field measurements tend to be sparse in both space and time in many northern countries. Here, we present an application of L-band frequency Global Navigation Satellite System (GNSS) Interferometric Reflectometry (GNSS-IR) for the estimation of lake ice thickness. The proof of concept is demonstrated through the analysis of Signal-to-Noise Ratio (SNR) time series extracted from Global Positioning System (GPS) constellation L1 band raw data acquired between 8-22 March (2017 and 2019) at 14 lake ice sites located in the Northwest

[2] Some citations and style formatting changes have been made to the journal version to make the paper consistent with the requirements of the thesis format.

Territories, Canada. Dominant frequencies are extracted using Least Squares Harmonic Estimation (LS-HE) for the retrieval of ice thickness. Estimates compare favorably with in-situ measurements (mean absolute error = 0.05 m, mean bias error = -0.01 m, and root mean square error = 0.07 m). These results point to the potential of GPS/GNSS-IR as a complementary tool to traditional field measurements for obtaining consistent ice thickness estimates at many lake locations, given the relatively low cost of GNSS antennas/receivers.

Keywords: GNSS, GPS, interferometry, reflectometry, lake ice thickness

3.2. Introduction

Lake ice is a significant landscape feature in the winter season at northern latitudes and plays a key role in climate moderation and the energy balance (Brown & Duguay, 2010). Lake ice conditions, notably the length of the ice season and ice thickness, have a significant impact on the economy of northern regions through their influence on transportation, travel, fishing, and recreation activities (Knoll et al., 2019). Therefore, accurate knowledge about lake ice properties, such as thickness, is necessary. However, manual measurement of ice thickness is time-consuming and can be expensive to perform in remote locations. Automated approaches are a possible alternative. For example, upward facing sonar systems such as the shallow water ice profiler (SWIP) have been used to obtain lake ice thickness throughout the ice season at both temperate and subarctic latitude (Brown & Duguay, 2011b; Murfitt et al., 2018). Ground-based radar systems such as Frequency-Modulated Continuous-Wave (FM-CW) radar have also proven effective for obtaining ice thickness at X- and Ku-band (Gunn et al., 2015). However, these systems are pricey to both acquire (e.g. tens to hundreds of thousands of dollars) and deploy at multiple locations.

Furthermore, while satellite retrievals of ice thickness from passive microwave and radar altimetry missions can provide reasonable estimates (root mean square errors ca. 0.15-0.30 m and correlations > 0.65), these methods are limited to larger lakes due to the low spatial resolution of the associated sensors (ca. km to tens of km footprints) (Kang et al., 2014; Beckers et al., 2017). Therefore, there is the need for a lower cost solution that can provide high-resolution estimations of ice thickness.

Non-positioning applications of Global Navigation Satellite System (GNSS) are frequently used as a low-cost method in various domains of application (e.g. atmospheric and surface monitoring). GNSS Interferometry Reflectometry (GNSS-IR) is one of the most common remote sensing approaches among non-positioning GNSS applications to measure surface properties, including soil moisture content (Chew et al., 2013), snow depth (Larson, 2016), and vegetation water content (Larson, 2016). Although the potential of GNSS-IR for sea ice detection (Strandberg et al., 2016) and ice thickness estimation (Jacobson, 2010; 2015) has been explored, there has been no direct field application for measurements over ice cover at multiple lake sites.

In this letter, we demonstrate and suggest the potential use of permanent or semi-permanent GNSS-IR stations for estimating lake ice thickness using data acquired during March 2017/2019 field campaigns at 14 sites in the Northwest Territories, Canada. GNSS antennas/receivers were installed concurrently near locations where manual ice thickness measurements were made. The dominant frequencies of signal-to-noise ratio (SNR) of reflected signals from the Global Positioning System (GPS) constellation are extracted using Least-Squares Harmonic Estimation (LS-HE) method to estimate the vertical distance from the reflective surface, which is derived from the distance between the GPS antenna phase centre and the ice-water interface. Ice thickness retrievals are shown to be in good agreement with in-situ measurements.

3.3. Methodology

3.3.1. Ice thickness retrieval from SNR

The SNR can be derived from the raw data recorded by any GNSS receiver. According to (Larson 2016), SNR has a sinusoidal form that varies with satellite elevation angle (e) and can be written as follows:

$$SNR = A(e)sin\left(\frac{4\pi H}{\lambda}\sin(e) + \phi\right) \quad (14)$$

where A(e), H, and ϕ denote amplitude, antenna height and phase shift, respectively. The carrier wavelength is represented by λ, which is 19 cm for GNSS L1 band. Next, the frequency ($4\pi H/\lambda$) is estimated using univariate LS-HE as suggested in (Amiri-Simkooei et al., 2007) to retrieve the antenna height from the reflective surface. The periodogram presented in Figure 3.1 is the output of the LS-HE method where the major peaks represent the distance between the antenna phase centre and the ice-water interface. Readers are referred to Larson (2016) for further details on the approach. This example of frequency waveform was obtained from the SNR time series recorded by the GNSS receiver at Waite Lake (Site ID 6; see Figure 3.3 and Table 3.1) with dominant peaks related to the vertical distance between the antenna phase centre and the reflecting surface. Since the GNSS antenna is installed on the ice surface, the antenna phase centre height (i.e. the distance between the antenna phase centre and the ice-water interface) shown by the waveform is used to estimate total ice thickness. However, because the antenna phase centre is located above the ice surface, an offset must be applied to estimate ice thickness. For this example, an antenna phase centre height of 0.75 m was retrieved. After applying the offset, ice thickness was determined to be 0.68 m, while the manual field measurement was 0.73 m.

The reasons that LS-HE is preferred rather than any other periodogram, such as the Fourier transform, are twofold: (1) the time intervals between data sampling do not need to be equal, and (2) other dominant frequencies can be used to obtain the antenna height from multiple reflective layers. However, in the present study, the only layer considered as the reflective surface is the ice-water interface since it is known that the L-band signal penetrates well into the freshwater ice column overlain by dry snow (Cardellach et al., 2012; Engram et al., 2013) and the dominant reflection is at the ice-water interface due to the large dielectric contrast between the two layers. Figure 3.2 illustrates the principle behind the GNSS-IR retrieval method for ice thickness estimation during the ice growth season.

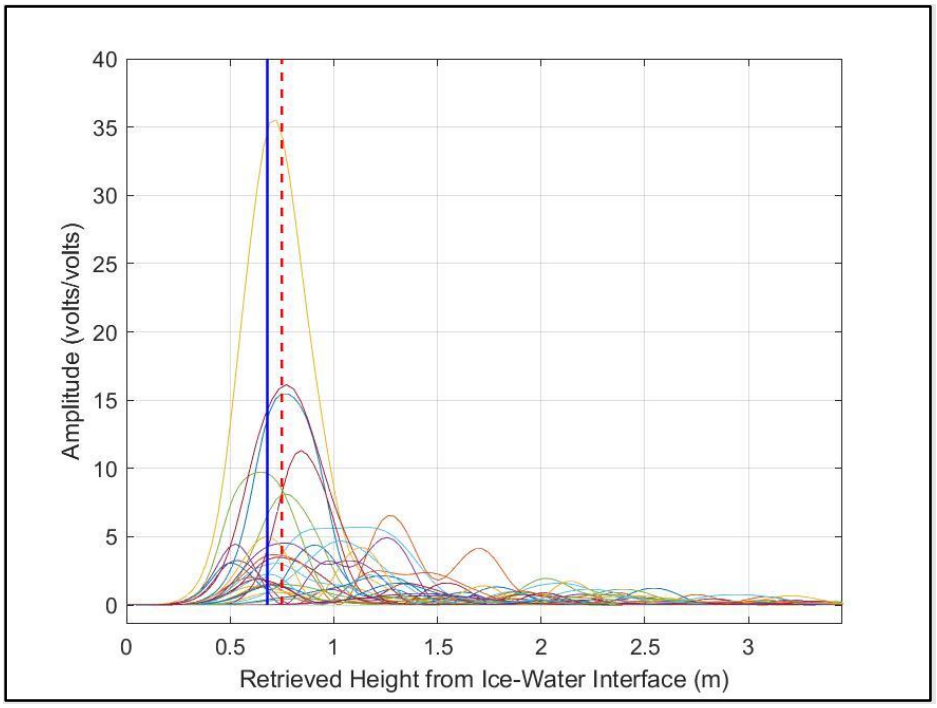

Figure 3.1. SNR spectrum obtained by LS-HE for a GNSS antenna installed on the top of the ice surface at Waite Lake (Site ID 6 in Table 1). Different colors represent the spectrum from different satellites. The dashed red line shows the median of the dominant peaks obtained from each satellite and is determined to be the antenna phase centre (the distance between the antenna phase centre and the ice-water interface) height (0.75 m). The solid blue line shows the estimated ice thickness of 0.68 m following application of the offset to account for the distance between the ice surface and the antenna phase centre.

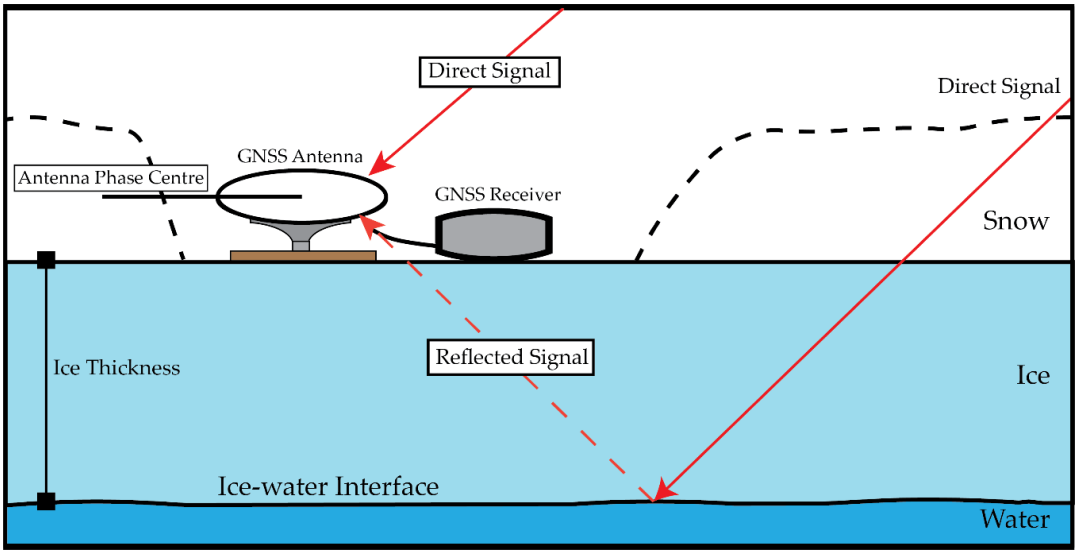

Figure 3.2. Principle behind the GNSS-IR retrieval approach for the estimation of ice thickness showing the GNSS reflected signal at the ice-water interface.

3.3.2 Experiment setup

GPS data were collected from modular (antenna and receiver) GNSS stations installed close to locations of manual ice thickness measurements between 8-22 March in 2017 and 2019. The systems were not initially deployed for GNSS-IR purposes, but rather as control points in support of airborne and satellite synthetic aperture radar (SAR) investigations on lake ice. GNSS antennas/receivers were installed at 14 lake ice sites located in the Northwest Territories, Canada (Table 1). The systems consisted of dual-frequency TRIMBLE NETR9 receivers and AshTech Pinwheel (model ASH701975.01A) antennas with 1 Hz sampling rate. Snow was cleared from a roughly 1x1 m patch so that the antenna could be placed directly on the ice surface (phase centre situated 0.071 m above the top of the ice surface) (Figure 3.4). Since reflected signals at low elevation angles easily interfere with line-of-sight signals (Zhou et al., 2019), data were collected only from GPS satellites from low elevation angles (5 to 30°). The software package introduced

in (Roesler and Larson, 2018) was used to extract SNR data from raw data files. Based on the average ice thickness of 0.88 m measured from all sites, the first Fresnel zone has a major axis length of about 20.22 m and a minor axis length of about 1.76 m with the lowest GPS satellites elevation angle of 5°, and 1.21/0.61 m (major/minor axis) with the larger elevation angle of 30^{o}. The process described in Section 2.1 was used to estimate ice thickness for all sites. Manual measurements of ice thickness were taken by drilling boreholes in the ice using ice augers. Ice thickness was determined using a tape measure with an ice thickness gauge to the nearest 0.01 m. Meteorological data for 2017 and 2019 were extracted for the two Environment and Climate Change Canada (ECCC) stations nearest the study sites, "Inuvik Climate" and "Yellowknife Airport" to identify days experiencing above-freezing air temperatures that could have an impact on the quality of GPS ice thickness retrievals.

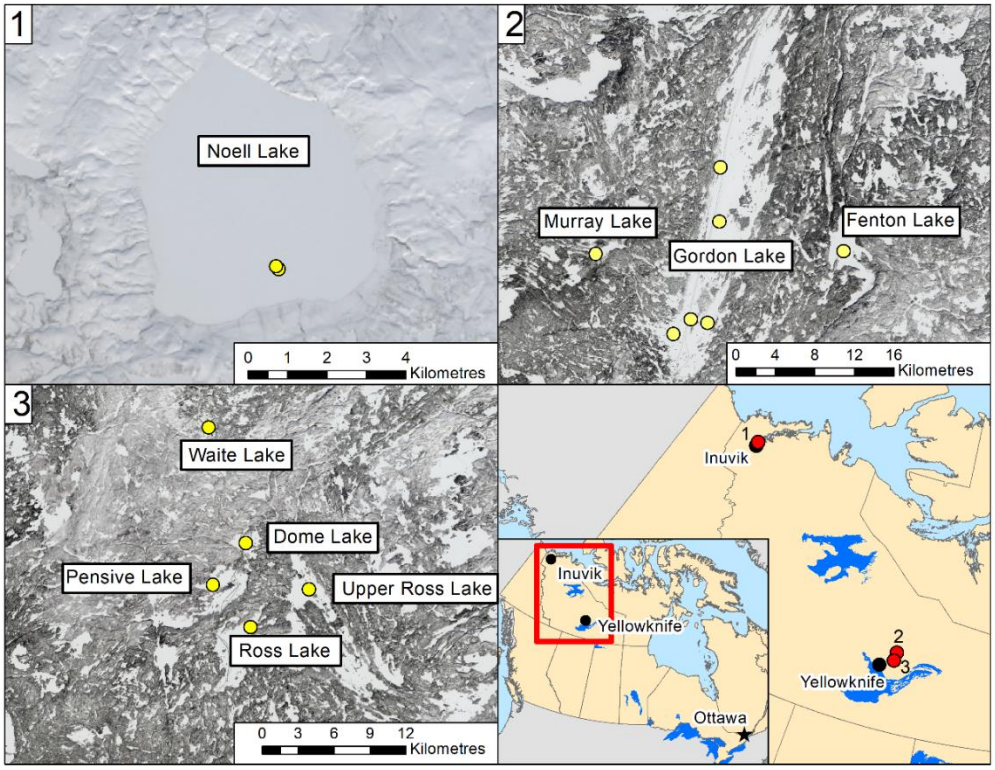

Figure 3.3. Location of modular GNSS stations deployed at lake ice sites, Northwest Territories, Canada.

Figure 3.4. GNSS antenna and receiver setup on the lake ice surface.

Table 3.1. General description of field sites along with corresponding geographical coordinates, deployment dates and ice thickness measurements from drilled boreholes.

GPS Site ID	Lake Name	Geographical Coordinates (dec. deg.)		Date	Measured Ice Thickness (m)
		Latitude	Longitude		
1	Gordon Lake	63.04556	-113.2169	9 Mar 2017	0.82
2	Gordon Lake	62.95611	-113.2667	10 Mar 2017	0.90
3	Gordon Lake	63.09444	-113.2186	8 Mar 2017	0.88
4	Gordon Lake	62.95361	-113.2331	10 Mar 2017	0.86
5	Gordon Lake	62.9425	-113.3003	14 Mar 2019	1.02
6	Waite Lake	62.8475	-113.3236	16 Mar 2019	0.73
7	Pensive Lake	62.73028	-113.3075	17 Mar 2019	0.80
8	Murray Lake	63.01222	-113.4606	12 Mar 2019	0.86
9	Ross Lake	62.69942	-113.24374	17 Mar 2019	0.94
10	Dome Lake	62.76222	-113.2561	18 Mar 2019	0.79
11	Fenton Lake	63.02222	-112.9669	14 Mar 2019	0.85
12	Upper Ross Lake	62.72933	-113.15086	17 Mar 2019	1.02
13	Noell Lake	68.51149085	-133.549	21 Mar 2019	0.89
14	Noell Lake	68.51185952	-133.551323	22 Mar 2019	0.89

3.4. Results and Discussion

Following the retrieval procedure described in section 3.3.1, ice thickness was estimated at each of the 14 sites (Figure 3.5). All sites combined, the mean absolute error (MAE) is 0.05 m, mean bias error (MBE) is -0.01 m, and the root mean square (RMSE) is 0.07 m. The obtained RMSE from this method is an improvement compared to best estimates of ice thickness from Great

Bear and Great Slave Lakes, which showed an RMSE of 0.19 m (Kang et al., 2014). The negative MBE indicates slight underestimation of retrieved ice thicknesses overall. The correlation between in-situ measurements and GNSS-IR retrievals is 0.66 (Figure 3.6), which is significant at 5% level and fits in the range for previous satellite-based estimates at > 0.65 (Beckers et al., 2017).

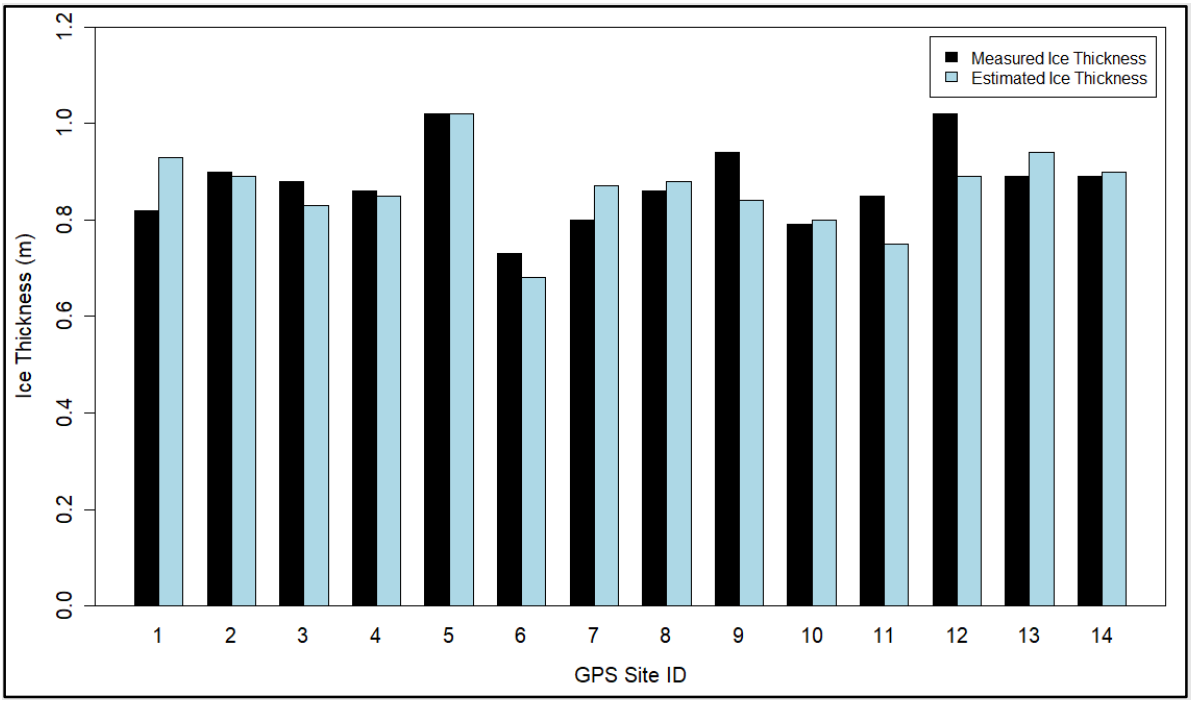

Figure 3.5. Comparison between estimated ice thickness from GPS-IR and measured ice thickness at each site location.

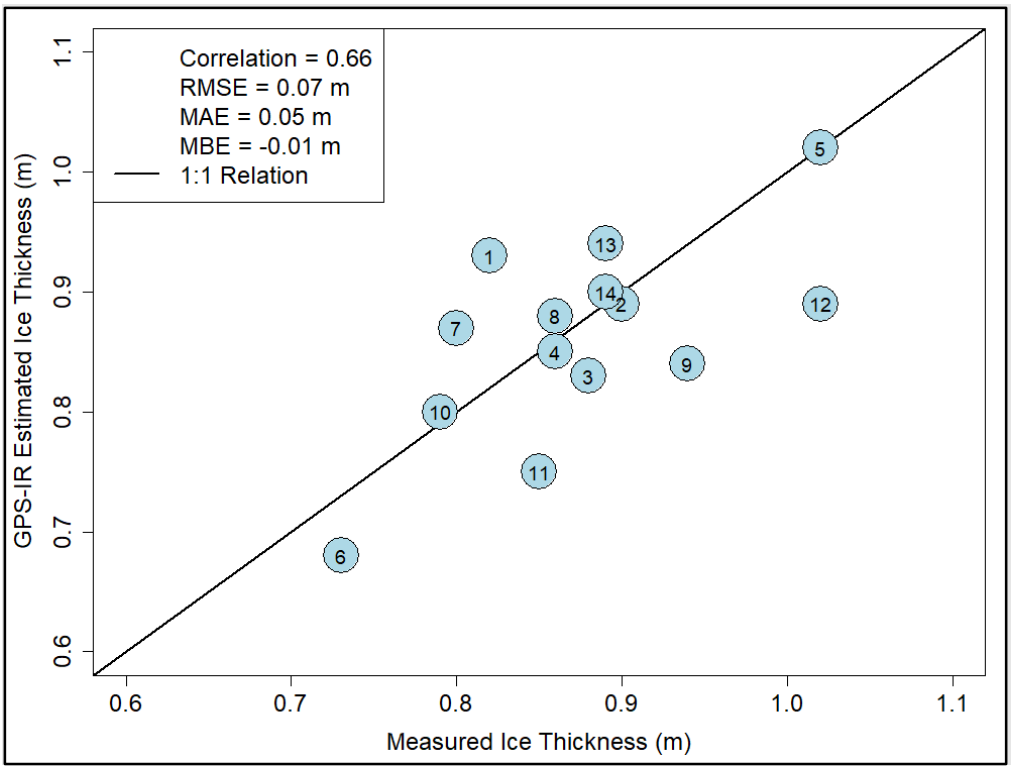

Figure 3.6. Correlation between in-situ measurements and GPS-IR retrievals.

Temperature records from the two ECCC stations provide insight into likely sources of larger error observed for some retrievals. These stations show that temperatures during or 2-3 days prior to coincident GPS-IR and ice thickness measurements reached 0 °C or above, particularly for sites at Ross and Upper Ross Lake (sites 9 and 12) (Figure 3.7). Above-freezing daytime (maximum) temperatures lead to melt followed by possible refreezing (minimum) at night. These conditions affected the GPS signals leading to larger retrieval errors (maximum of 0.13 m) as these temperature fluctuations during the 2019 field campaign resulted in snow surface melt and possibly within layers above the ice surface. These layers have a higher water content and act as additional sources of L-band reflection for direct GPS signals. Therefore, this added reflection can add noise to the measured signals and cause a decrease in the accuracy of the estimation of ice thickness. This was not found to be an issue for data collected in 2017, as the average temperature was

recorded as -22.6°C. Roughness of the ice-water interface may have an impact on the retrieved estimates. However, for the purpose of this research letter, the interface was assumed planar. Roughness of the ice-water interface for lake ice is difficult to retrieve and is an area of ongoing research. While other factors (i.e. snowpack and ice structure) may have affected the accuracy of estimated values (sites 1 and 11), further field information is needed to understand the extent of this impact and should be an area of future study.

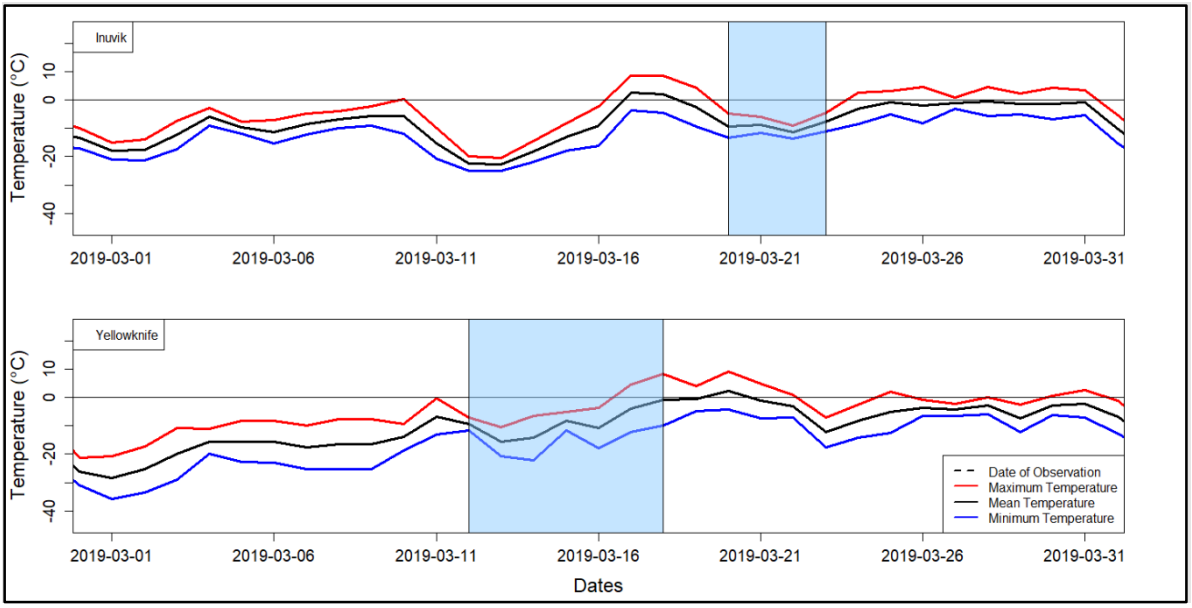

Figure 3.7. Maximum, minimum, and mean air temperatures recorded at Inuvik (top panel) and Yellowknife (bottom panel) during the 1 January - 31 May 2019 period. Shaded boxes correspond to field measurement periods when GPS data and ice thickness measurements were collected.

3.5. Conclusions and Future Work

In addition to other applications examined up until now, this study suggests that GPS/GNSS-IR can be employed as a low-cost and reliable remote sensing approach to estimate lake ice thickness. This method is also beneficial over spaceborne passive microwave estimates of ice thickness as it allows for finer-scale estimates and can be used for small and medium size lakes.

Among different frequency retrieval methods, LS-HE is used in this experiment, because it allows for the use of data at unequal time intervals. Ice thickness was estimated using a GNSS-IR approach at 14 lake ice sites and compared to in-situ measurements. The RMSE of the results is 0.07 m, the MBE is -0.01 m, and the MAE is 0.05 m, which is an improvement compared to previous estimates on large lakes made using passive microwave and radar altimetry data (Kang et al., 2014; Beckers et al., 2017). Moreover, a correlation of 0.66 is found between GPS-IR retrievals and in-situ measurements. Temperature records from weather stations located close to the locations show that higher temperatures, which can lead to snow surface melt and produce layers with higher water content, likely impacted the accuracy of ice thickness estimation. Further development of this method could allow for the development of a network of GNSS-IR station that may supplement current measurements of ice thickness along crucial ice routes.

It is also worth noting that this study focused on measurements at high-latitude lake sites that experience more consistent (colder) winter conditions compared to mid latitudes. At lower latitudes, mid-winter thaw and rainfall events are more common throughout the winter season (Ariano and Brown, 2019). This means that unlike the lakes presented in this study, where the main reflective surface was the ice-water interface as expected under cold conditions, additional reflective surfaces (slush/water layers, ice layers in the snowpack, and varying ice types) may be present in the snowpack or upper ice layers of lake ice cover at lower latitude lake locations. These effects should be studied in future research. Moreover, measurements were only obtained during late-winter field campaigns (March 2017 and 2019); therefore, a limitation of this study is that we do not know with certainty how well the retrieval approach would perform from initial ice formation with thin ice in late-fall/winter until just before melt onset in spring. Although the correlation between estimated and measured ice thickness is relatively high and retrieval errors are

low, further research is needed to determine the consistency of the retrievals throughout the ice season.

Future experiments to expand on this novel work should involve the establishment of a semi-permanent station mounted on mast along the shore of a lake to observe the GNSS-IR reflected signals to lake ice throughout one or more full ice seasons. The additional height of the mast would allow for retrieval of ice thickness over a larger area compared to placing the antenna directly on the ice surface as was done in this initial experiment (Larson et al., 2020). Additionally, this setup can include tests of different antenna orientations, such as a side-looking antenna as described by (Alonso-Arrovo et al., 2015) or the three-antenna approach (one zenith and two side-looking) as described by (Cardellach et al., 2012). The establishment of a semi-permanent station would provide valuable information on how the approach proposed herein could be used to monitor lake ice growth and decay. Furthermore, supplemental field measurements would lead to a better understanding of how the GNSS-IR reflected signals are impacted by ice and overlying snow properties under colder and warmer weather conditions (e.g. snow surface melt, slushing at the snow-ice interface and snow-ice formation following refreeze of slushy layers) and uncertainty characterization in ice thickness retrievals. In addition to field measurements, forward modelling using radiative transfer models, such as the Snow Microwave Radiative Transfer (SMRT) model (Picard et al., 2018), will help to further identify uncertainties in the estimate of ice thickness. An assessment of the various sources of uncertainty is a necessary step towards the implementation of a GNSS-IR network of stations where lake ice thickness estimates could be obtained on a regular basis across various regions of northern countries such as Canada.

Chapter 4 – GNSS-IR experiment at MacDonald Lake, Ontario, during ice season 2019-2020

This chapter is a logical extension of the GNSS-IR experiment described in Chapter 3. It presents results of an experiment in which a time-series of GNSS-IR observations was collected at a mid-latitude lake location over the full ice season of 2019-2020. In addition, the capability of GNSS-IR for estimating the depth of multiple (reflecting) layers of lake ice and the overlying snowpack is investigated. This chapter contains: (1) a description of the experimental setup and data collected for this study; (2) results of the experiment, and (3) a discussion and interpretation of results.

4.1. Experimental Setup and Data

This study was conducted on the southwestern shore of MacDonald Lake (Haliburton, Ontario) from November 19, 2019 to March 9, 2020. The main setup of this experiment was the installation of a GNSS tower on the shore to collect reflectometry data from the lake surface over a full ice season. The tower was installed next to a weather station operated by the group of Dr. Laura Brown (University of Toronto Mississauga) that records amongst other variables air temperature and snow accumulation on the ground. In situ ice and snow measurements were also carried out within the footprint of reflected signals measured by the GNSS unit on a bi-weekly basis for validating ice thickness and snow depth estimates obtained from GNSS-IR. Figure 4.1 shows the study area and the location of the experimental setup on the southwestern part of the lake. A description of instrument installation as well as the primary (GNSS signals) and secondary sources data are provided next.

4.1.1. GNSS signals

The primary equipment for this study was a GNSS antenna-receiver unit installed on a 5-meter tower on the shore of MacDonald Lake (Figure 4.2). The unit is a Reach RS+ model manufactured by the Emlid Company in 2019. More details on the GNSS unit can be found at https://emlid.com/reachrs+/. The power supply of the unit is a 12V marine battery, which kept the unit collecting signals continuously. Using equation (7) presented in section 2.3 and considering 5-25^{o} for satellites elevation angle range, one can calculate the area of the footprints of the GNSS reflected signals, which is determined to cover an area of a radius of ~151m over the lake surface.

The unit was setup to receive GNSS signals at a 1 Hz sampling rate. This unit is able to write and store data in both raw and RINEX file formats (see section 2.2.1 for details). To extract SNR values from daily RINEX files, the software package introduced by Roesler & Larson (2018) was used. The SNR files were processed subsequently using a MATLAB code developed by the author to extract heights at various time intervals (daily, 12-hour and 6-hour basis) through implementation of the LS-HE method described in sections 2.4.1 and 2.4.2.

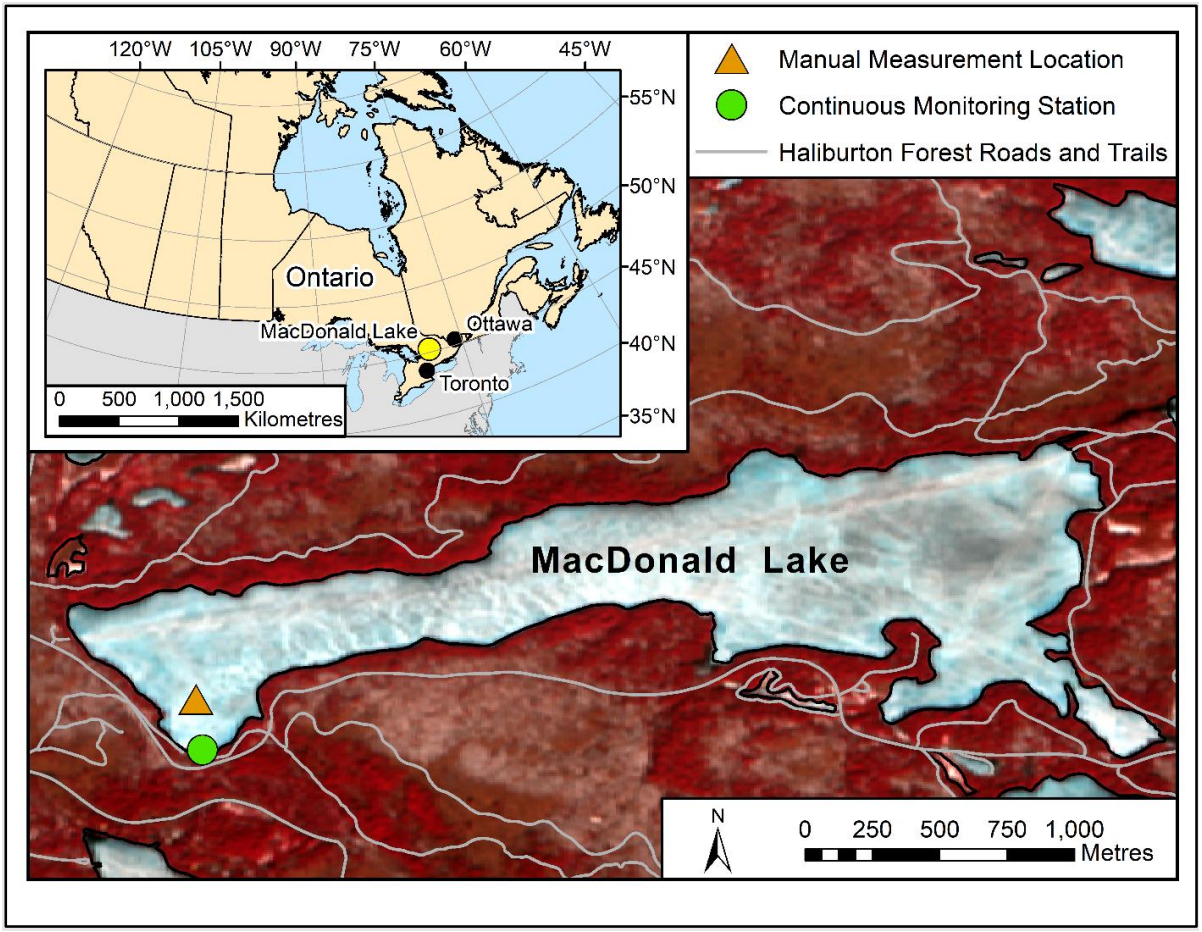

Figure 4.1. Location of MacDonald Lake as well as the location of GNSS/weather stations (continuous monitoring station) and in-situ measurement site. The background image is from the Sentinel-2 satellite (acquired on April 6, 2020) displayed as a false color composite.

Figure 4 2. GNSS tower installation on the shore of MacDonald Lake on November 19, 2019.

4.1.2. Meteorological data

Meteorological data were acquired from a weather station mounted on the shore of MacDonald Lake by the University of Toronto in fall 2015. Among various measurements collected at station are air temperature and snow depth data sampled on the hourly basis, which were used in this study. Air temperature data is the only input for the estimation of ice thickness using Stefan's equation. Despite the existence of more complex models using multiple factors to estimate ice thickness (e.g., snow depth and snow density), the modified Stefan's equation is a

simple equation that uses only one input variable (air temperature), in which environmental conditions can be reflected through coefficients fit to curves obtained from in-situ measurements. The simplified form of Stefan's equation to estimate ice thickness during the ice growth period is as follows (Lebedev, 1938):

$$h_i = \beta_F * AFDD^{\gamma} \quad (16)$$

where h_i is the ice thickness and $AFDD$ stands for the accumulated freezing degree days, which are calculated once daily temperature values are constantly below 0°C . The coefficients β_F and γ reflect the environmental conditions affecting the ice growth, such as the average snow accumulation. It should be noted that the ability of Stefan's equation for simulating ice growth on MacDonald Lake has been demonstrated and coefficients were tuned for this lake based on in situ measurements from a recent study (Murfitt et al., 2018). According to this study, the optimized values for β_F and γ for MacDonald Lake are 1.73 and 0.5, respectively. Furthermore, over-land snow accumulation data are used as a control to validate the general pattern of over-ice snow accumulation obtained from the GNSS-IR tower.

4.1.3. In-situ ice and snow measurements

As another ground-truth control, we measured ice thickness manually during four field visits inside the GNSS footprint area by drilling the ice at nine locations (Figure 4.1) and deriving the average ice thickness values from each visit. Snow depth and snow density (at different depths along the snow profile) were also measured. These measurements played an important role in the interpretation of the reflected signals obtained from GNSS-IR.

Manual measurements of ice thickness were taken by drilling boreholes in the ice using a 1-meter length Kovacs© auger. Ice thickness was then measured to the nearest 0.01 m using a tape

measure. In addition, snow depth measurements were obtained using a metal ruler placed vertically into the snowpack to reach to the ice surface. Snow density was also determined at each point by weighing a known volume of snow grabbed by means of a PVC pipe with known diameter.

4.1.4. Canadian Lake Ice Model (CLIMo)

CLIMo is a one-dimensional model developed to simulate ice phenology and thickness on lake ice. Atmospheric forcing (input) variables include mean daily air temperature, wind speed, snowfall, relative humidity, and cloud cover (Duguay et al., 2003). Calculating an energy budget and net flux, and using finite difference approach, CLIMo solves the one-dimensional heat conduction problem and determine the thickness and temperature of different layers of snow and ice.

Using the MacDonald and Haliburton 3 weather station data (air temperature, relative humidity, snow depth, and wind speed) as well as hourly cloud cover data from the European Centre for Medium-Range Weather Forecast (ECMWF, ERA5) as input variables, a simulation was performed with CLIMo to obtain a time series of ice growth evolution. Aside from ice thickness, which can also be retrieved with the "tuned" Stefan equation for MacDonald Lake (see 4.1.2), CLIMo provides us with additional parameters, including on-ice snow depth and the temperature at different depths along the snow and ice profile, which are necessary in the assessment of retrieved snow depth and amplitude SNR values obtained from GNSS-IR. Figure 4.3 shows the ice thickness and snow depth obtained from a CLIMo run for the 2019-2020 ice season with of 200 kg m^{-3} (mean value for dry snow determined from field measurements) and a near-shore lake depth of 3 m.

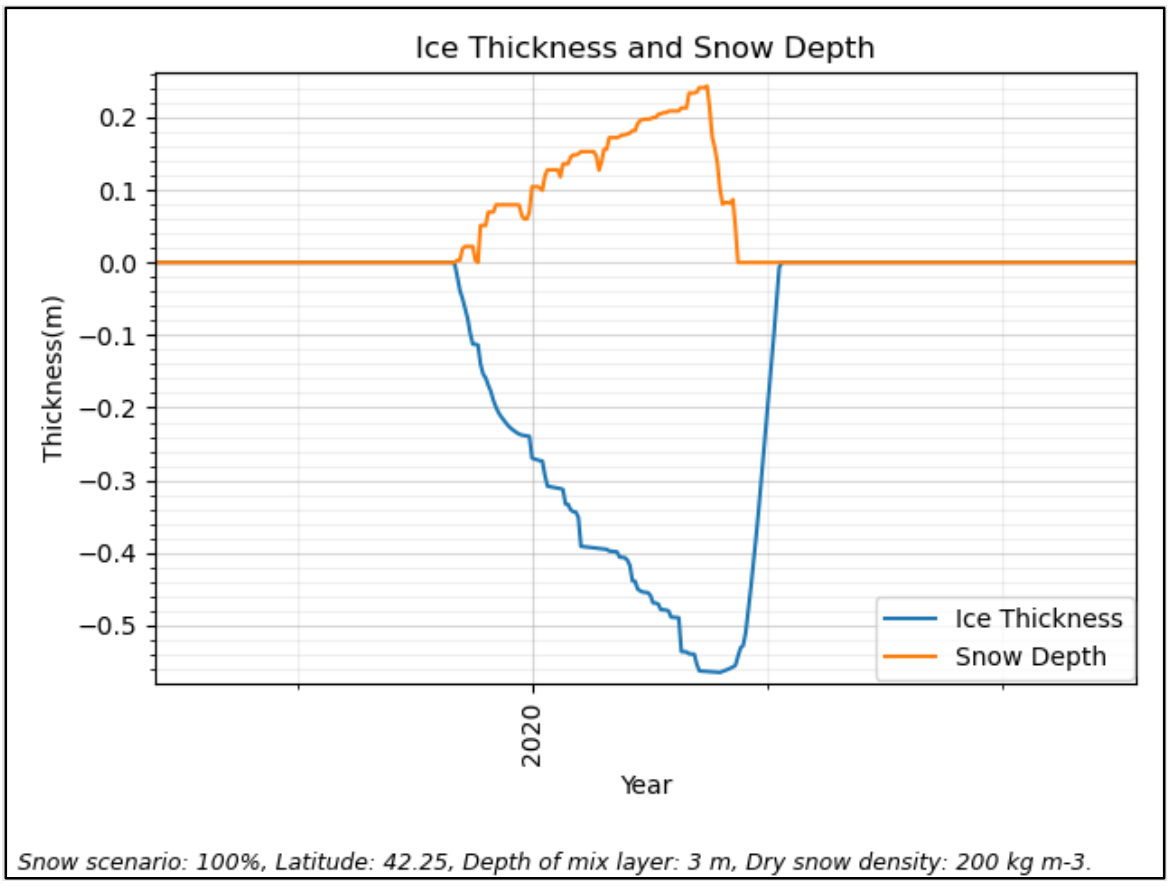

Figure 4.3. Ice thickness and snow depth time series for the 2019-2020 ice season obtained from CLIMo.

4.2. Results

Tower-based GNSS acquisitions took place between November 19, 2019 and March 9, 2020, which resulted in 112 daily RINEX files. Each RINEX file was processed following the procedure described in 2.3 and 2.4 to obtain SNR files, which include satellite number, time of observation, satellite azimuth and elevation angle, and SNR value for each observation. Afterwards, daily SNR files were split to 12-, 8-, 6-, 4- and 2-hour length SNR files to be analyzed separately. Running LS-HE in MATLAB 2019a, antenna heights from different reflective layers were then retrieved. The threshold for "the ratio of peak to background noise", which is the criteria for the frequency significance, was set to a value of 3.5 as suggested by other researchers (Roesler

& Larson, 2018). Performing LS-HE on SNR files, one can see that up to four significant frequencies and, by implication, four different layers can be achieved as will be shown next.

4.2.1. Lake ice evolution

Figure 4.4 shows the variation of the antenna heights from four layers based on the frequency values returned by LS-HE. Each subplot in Figure 4.4 is related to the length of observation period that the daily SNR files are split based on that time. For example, the subplot titled “6-Hour” means that for generating this figure, each daily SNR file is first split into 6-hour intervals, and then used as inputs for the LS-HE. The layer order described in the legend of Figure 4.4 is based on the number of significant frequencies retrieved from SNR files. Combining all retrievals shown in Figure 4.4, one can see the general pattern of lake ice formation obtained from the GNSS-IR tower, as depicted in Figure 4.5.

To observe the patterns more clearly, the average trend of all positive values is calculated and assumed as the top layer height for each given date and time, and the minimum of negative values is calculated and considered as the level of the bottom layer for each given time and shown in Figure 4.6.

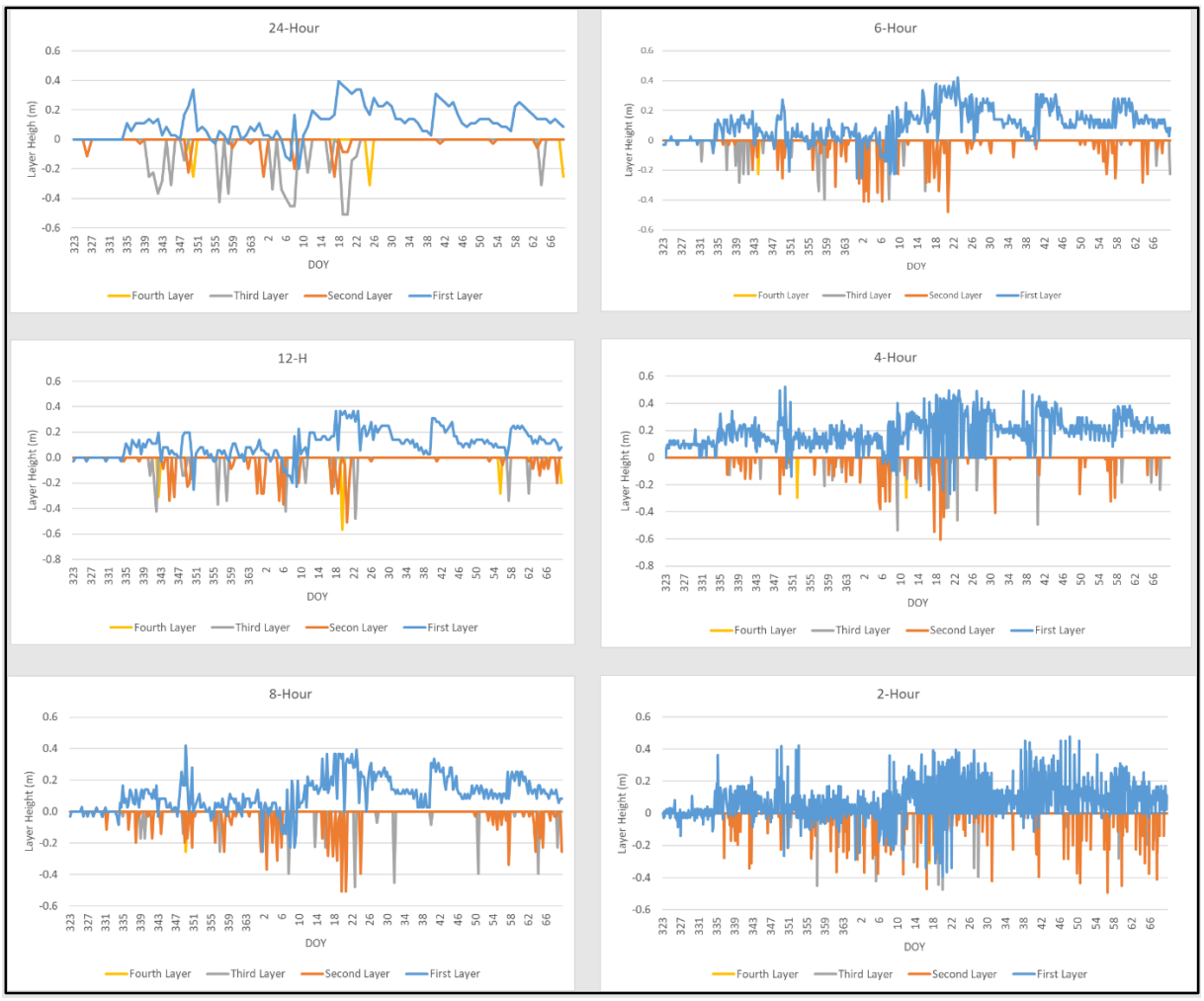

Figure 4.4. Antenna heights obtained from different reflective layers using GNSS-IR. The order of the reflections is obtained from the order of the frequencies shown in Figures 2.8 and 2.9 of section 2.4.

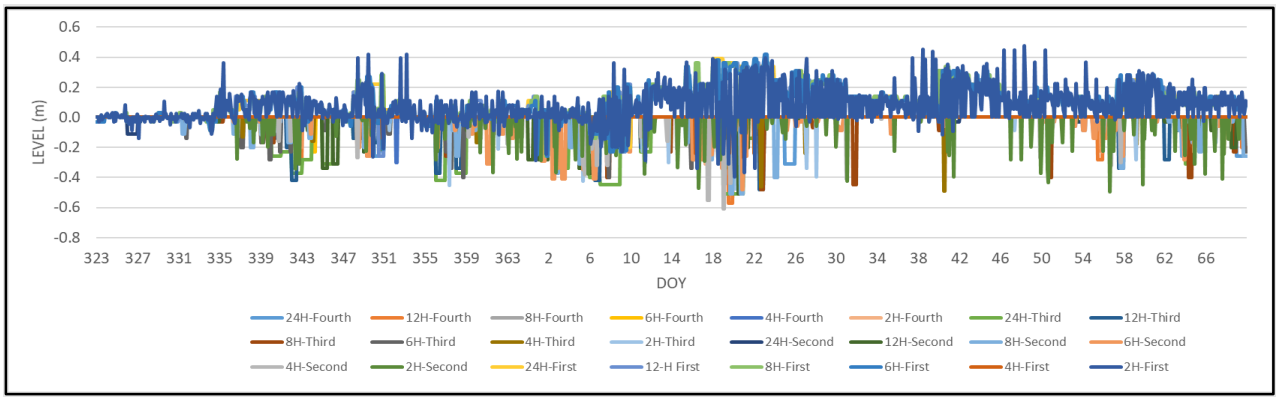

Figure 4.5. The combination of all retrievals from all SNR files with all intervals.

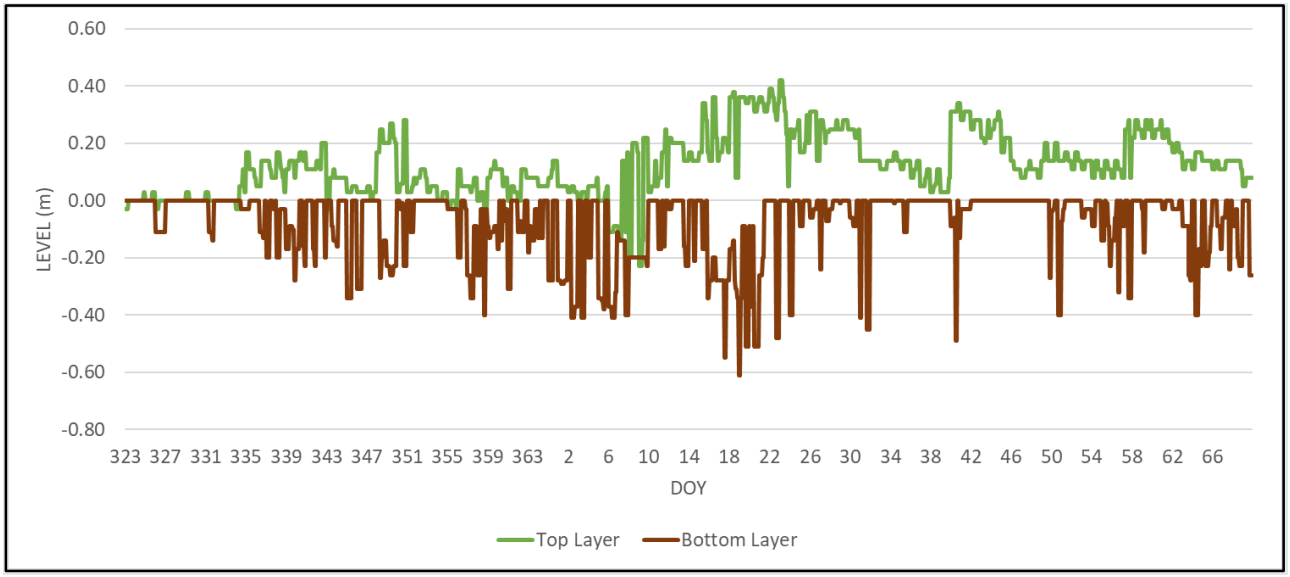

Figure 4.6. Two main layers retrieved from GNSS-IR.

4.2.2. Ice phenology timing

As demonstrated in section 2.3.2, the coherency of reflected GNSS signals increases as ice forms on the lake. Therefore, freeze-up timing can be determined by observing the power amplitude of the first frequencies, which represents the main reflection. Figure 4.7 shows the amplitude variation of the first frequencies obtained from daily SNR files. The largest values correspond to days of the year (DOYs) between 342 and 346 (December 8-12, 2019) which is just after the freeze-up period. Two Landsat-8 (panchromatic Band 8) images are shown in Figure 4.8

illustrating open water on November 30 (DOY 334), while the lake is completely frozen on December 7 (DOY 341). Therefore, one can conclude that the freeze-up occurred sometime between these two dates. However, days could not be obtained during the break-up period because of the experiment was terminated due to the COVID-19 pandemic.

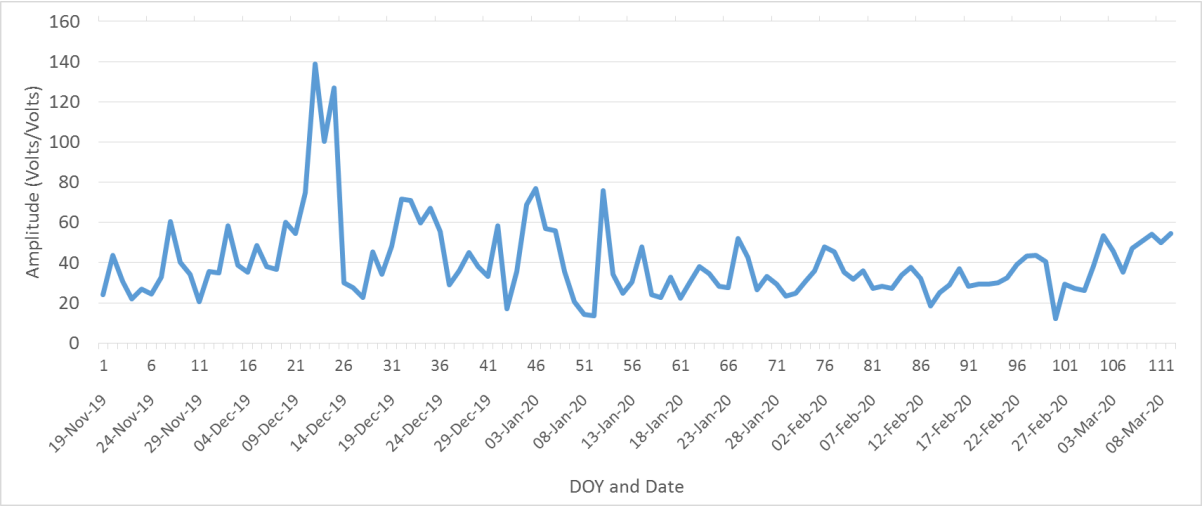

Figure 4.7. Variations in amplitude of the first frequency over the time.

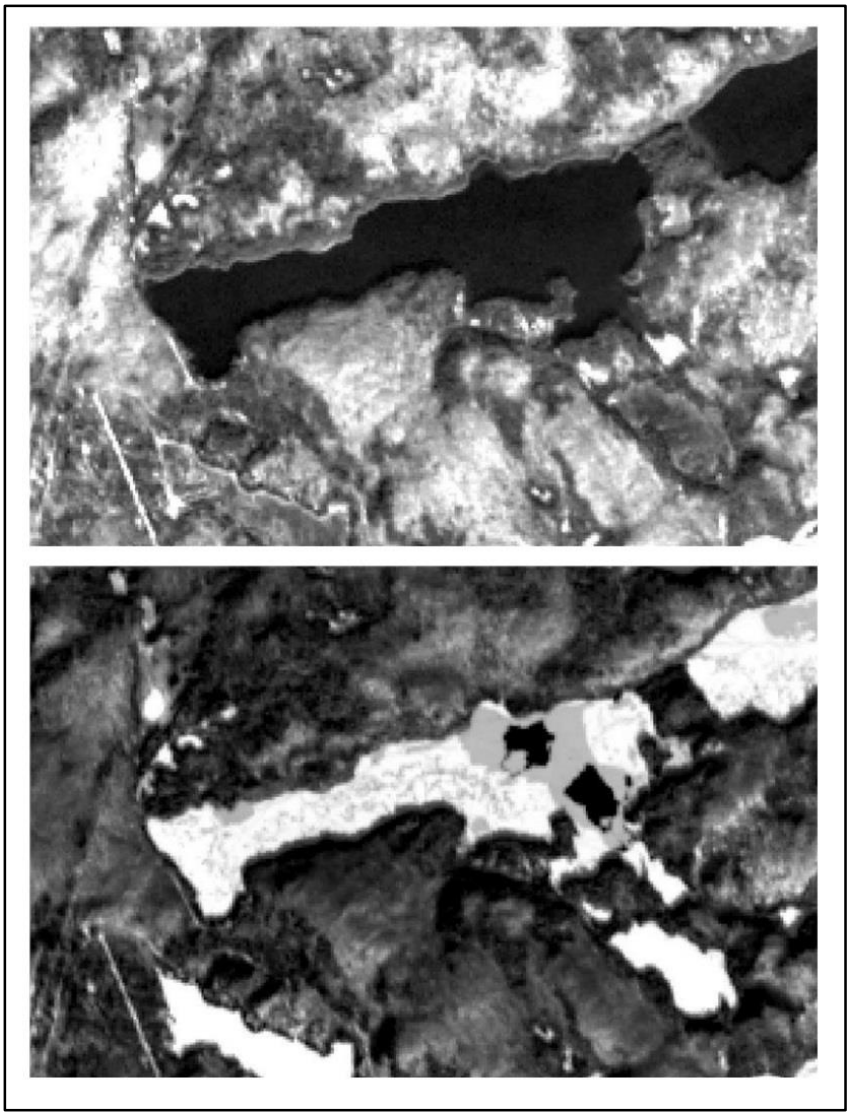

Figure 4.8. Lake status on (top) November 30, which is open water, and (bottom) December 7 which is completely frozen at the GNSS tower coverage area. Images are obtained from Landsat-8.

4.3. Discussion

Based on results obtained and also shown in section 3.2, several outputs are achieved, which need to be interpreted and validated alongside supplementary data and in-situ measurements. This study was initiated to estimate lake ice thickness; however, the ice and snow

conditions at MacDonald Lake (a temperate lake) are such that it steers us into examining more features than at the sub-Artic lakes study described in Chapter 3, such as the impact of slush and wet snow on the GNSS signals. For instance, the slush layer, which is present on most days during the ice season, acts as a barrier to the GNSS signals as this wet layer does not allow the signals to reach to the bottom of the ice (i.e. ice-water interface). Therefore, only small or noisy reflections can be obtained from the bottom of the ice compared to the layers above. In this section, we will further discuss the effect of temperature, as the main effective driver in the appearance of wet layers, on the efficiency of GNSS-IR in lake ice studies.

4.3.1. Classification of layers

Two main layers are retrieved from the SNR files and their variation above and below the initial water level was shown in Figure 4.6. Variations in the height of these two layers are compared with simulated and field measurements of snow depth and ice thickness. Above or near the first layer, there are three layers: (i) snow depth on the ground, which is obtained from the weather station; (ii) snow accumulation on the lake ice surface obtained with CLIMo; and (iii) snow depth measured on the lake manually during the field visits. Similarly, there are three layers below the first layer is shown in Figure 4.9, including: (i) ice thickness retrieved from Stefan's equation; (ii) ice thickness obtained with CLIMo; and (iii) in-situ measurements of ice thickness made during field visits.

Comparing GNSS-IR retrievals with supplementary data and field measurements, one can see that GNSS-IR results, named the top layer and bottom layer in Figure 4.9, generally agree with snow accumulation and ice thickness data.

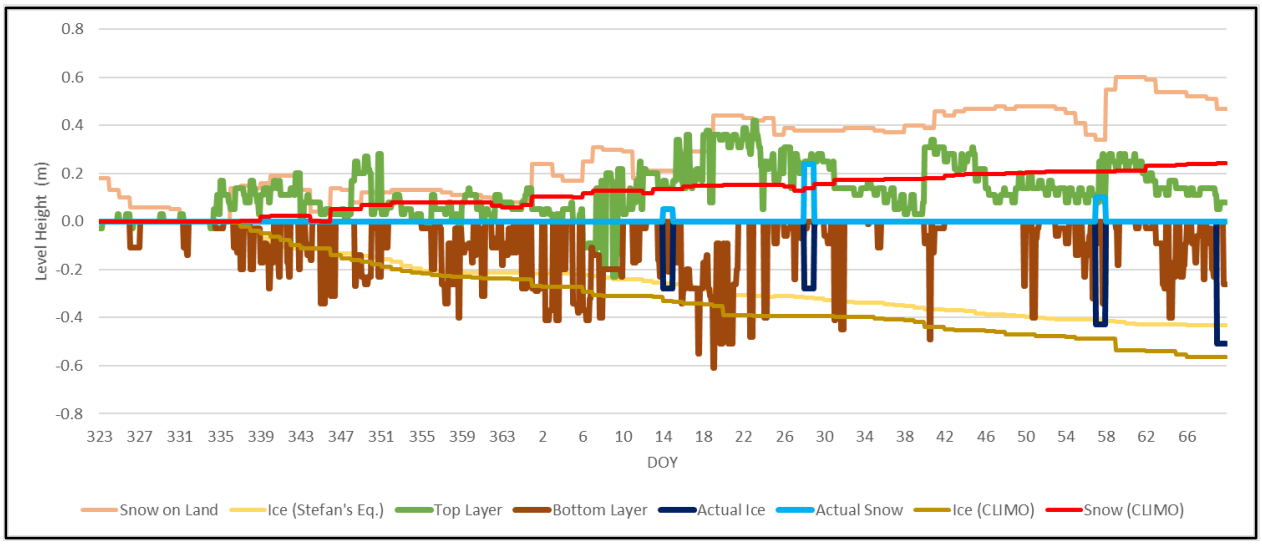

Figure 4.9. Comparison between retrieved layers shown in Figure 4.6 and supplementary data (model simulations and field measurements of snow depth and ice thickness).

4.3.1.1. Snow depth

The main evidence supporting the consistency of the "top layer" trend with snow accumulation is the variation of on-land snow depth values obtained from the MacDonald weather station. Looking at on-land snow variation, specifically on DOYs 335 to 343, and DOYs 26 to 66, one can see a tendency in the top layer trend to follow the on-land snow pattern. However, since the mass of snow on-ice may initiate snow-ice formation (see section 2.1.1), one can expect a lower level for the on-ice snow compared to the on-land snow. In addition, on-ice snow obtained from CLIMo supports the snow depth obtained from GNSS-IR as its trend is almost consistent with the average of GNSS-IR retrievals.

In addition, amongst the manual snow-depth measurements made during field visits, values from DOYs 28, 57, and 69 support well the GNSS-IR snow-depth retrievals. However, the in-situ snow measurement on DOY 14 (5 cm) is much less than what the GNSS-IR retrieved top layer

suggests. Overall, the top layer represents generally well the snow accumulation and its variation on the lake ice surface.

4.3.1.2. Ice thickness

The results shown as "bottom layer" in Figure 4.6 can be linked to ice thickness; however, it is not as straightforward as the top layer and snow depth results. Although the bottom layer is in general agreement with either supplementary ice thickness data (i.e. Stefan and CLIMo estimates), a number of inconsistencies can be occasionally observed in GNSS-IR results. DOYs 2 to 8, and DOYs 17 to 22, are examples of the overestimation, and, on the other hand, DOYs 63 to 69 are examples of the underestimation of the ice thickness. Potential reasons for these inconsistencies are discussed in next section based on the temperature variations and snow accumulation.

4.3.2. Temperature effect

According to the physics of L-band remote sensing, and as discussed in section 2.3.1, one expects more reflection from the ice-water interface and less reflections from other layers since the dielectric contrast is higher at the ice-water interface. However, with the appearance of wet layers in snow due to warm temperature and mid-winter melt, the dielectric difference changes as well and stronger reflections are received from these layers rather than the ice-water interface.

Figure 4.10 depicts temperature variations recorded at the weather station and GNSS-IR retrievals at the same time. In this figure, the top and bottom layers achieved from GNSS-IR are considered as retrieved snow and ice, respectively. Figure 4.11 shows the GNSS-IR results compared with surface temperature (top of the snow surface) and Level-1 (top of the ice surface) temperature estimated from CLIMo.

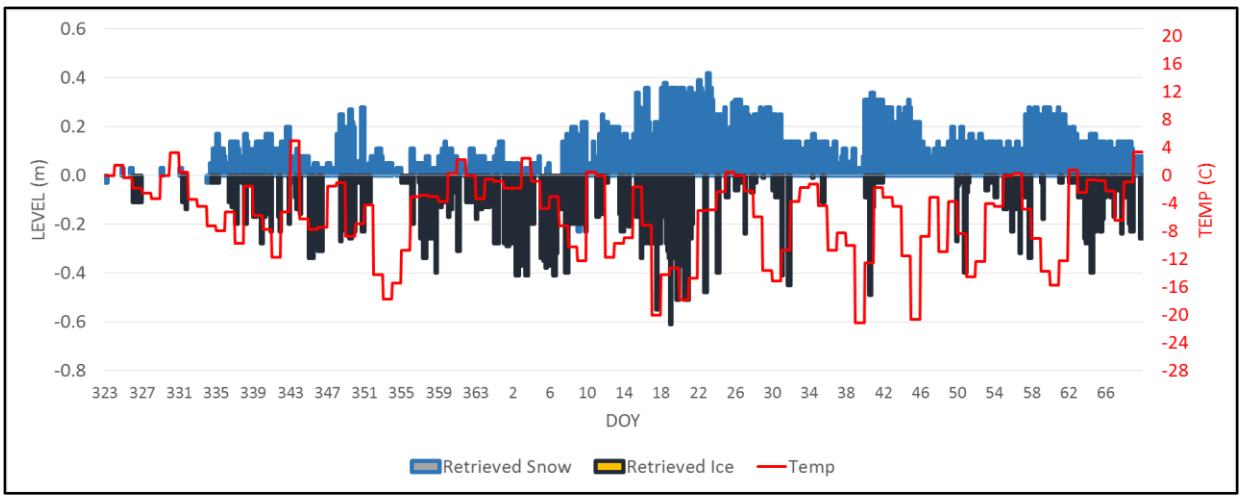

Figure 4.10. GNSS-IR retrievals accompanied with temperature data from the MacDonald weather station.

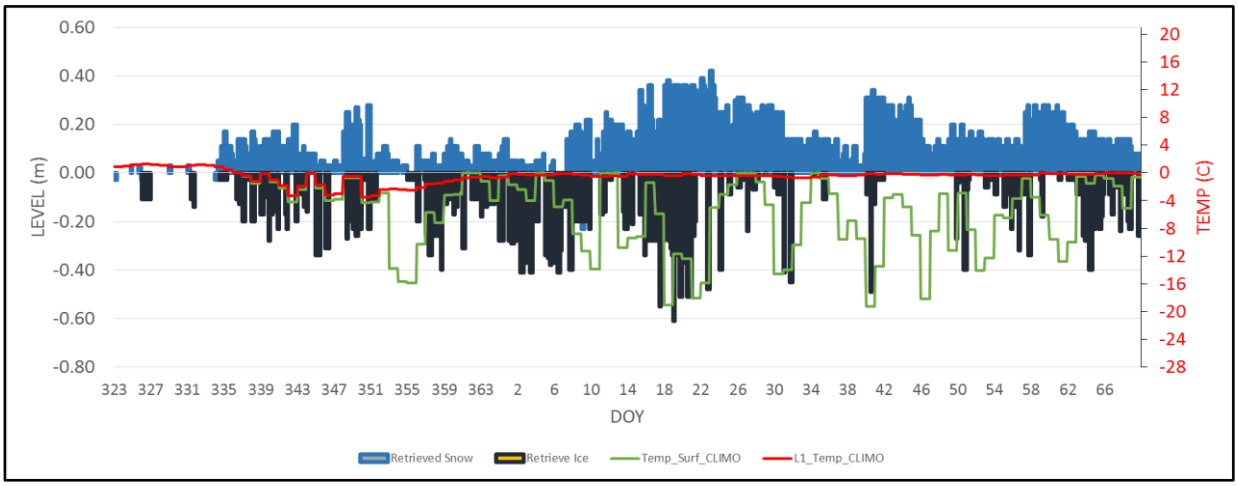

Figure 4.11. GNSS-IR retrievals accompanied with surface temperature and top-of-the-ice temperature from CLIMo.

There are several days during this experiment where temperatures oscillate near or above zero, which suggest mid-winter melt and wet layer formation inside snow and ice (slush/snow ice layers) columns. While there are large fluctuations in temperature shown in Figures 4.10 and 4.11, the GNSS-retrieved snow depth and ice thickness along with CLIMo simulations of Level-1 (top

of the ice surface) temperature suggest that the wet layers do not always totally refreeze. These wet layers are assumed to be present on most days of the experiment. As a result, these wet layers, which act as a barrier for GNSS signals, do not allow for the retrieval of ice thickness on several days of the ice season (see gaps in retrieved ice thickness time series).

These conditions largely explain the underestimation of the ice thickness on many days because the warm temperature brings about wet layers in the snowpack and slushing which is more prevalent with the additional mass of snow on the ice surface (increase in density from dry snow at 200 kg m-^{3} to wet snow at 450 kg m^{-3} in CLIMo). For instance, towards the end of the experiment (DOY 69), in which an above zero temperature was experienced, a water layer was indeed observed in the field inside the ice at the depth of 22 cm, which caused a reflection towards the GNSS-IR system. Therefore, GNSS-IR retrieved this value as the ice thickness, while the measured ice thickness as 51 cm (see Figure 4.9).

Furthermore, the warm temperature experienced during the experiment elucidates the reason for the dominancy of reflection from the top or inside the snowpack. While one would expect the prominent GNSS reflection to come from the ice-water interface, the main reflections, as shown in Figure 4.4, are usually received from the snowpack overlying the lake ice surface. Another evidence supporting the effect of temperature on the order of frequencies can be seen between DOYs 6 to 10, 18 to 23, 30 to 34 and 39 to 41, for example, when the weather was well below zero degrees for a few days in a row, and, as a result, water likely refroze inside the ice and snow columns. Thus, during those days, as shown in Figures 4.4 and 4.5, the main reflective layer is the bottom of the ice column, and the depth retrieved by GNSS-IR agrees relatively well with ice thickness values estimated by the lake models (see Figure 4.9).

Another impact of temperature on GNSS-IR retrievals can be seen in the variation of reflection power received from the lake ice previously shown in Figure 4.7. Comparing daily SNR amplitudes with the mean air temperature obtained from the MacDonald weather station one can see a significant effect of the temperature fluctuation on the SNR variation (Figure 4.12).

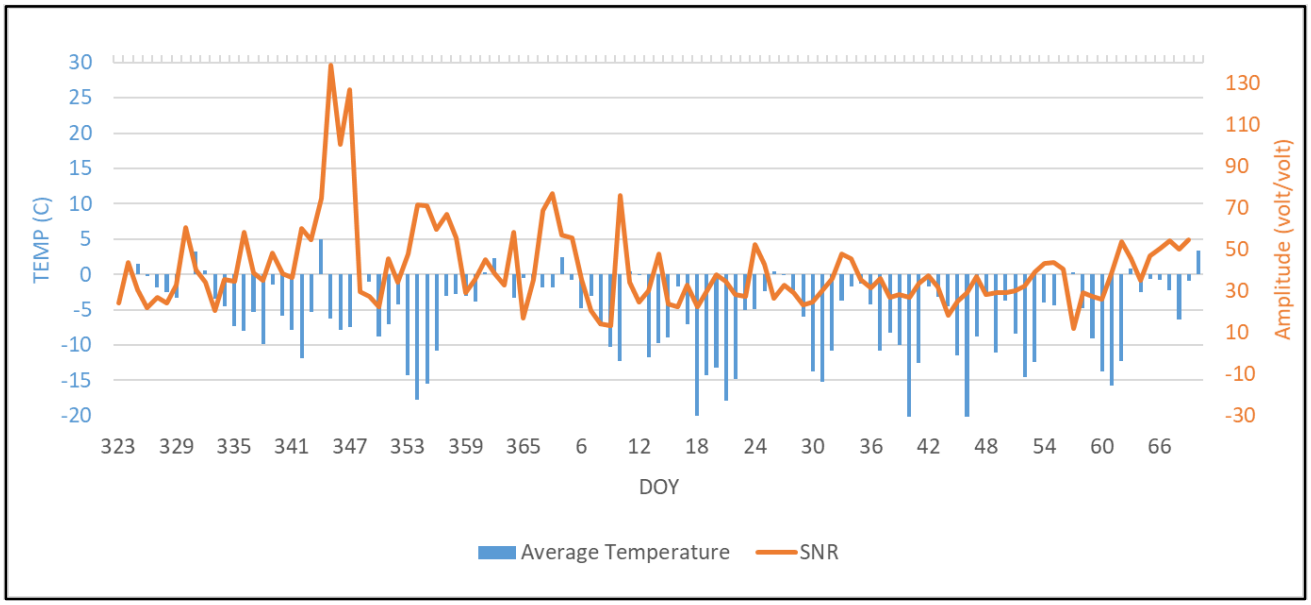

Figure 4.12. SNR amplitude and air temperature variations.

In Figure 4.12, a significant drop in SNR amplitude can be seen when the average air temperature is near or above zero. To better elucidate this effect, Figure 4.13 is provided to show the daily differences in SNR amplitudes compared to the average air temperature.

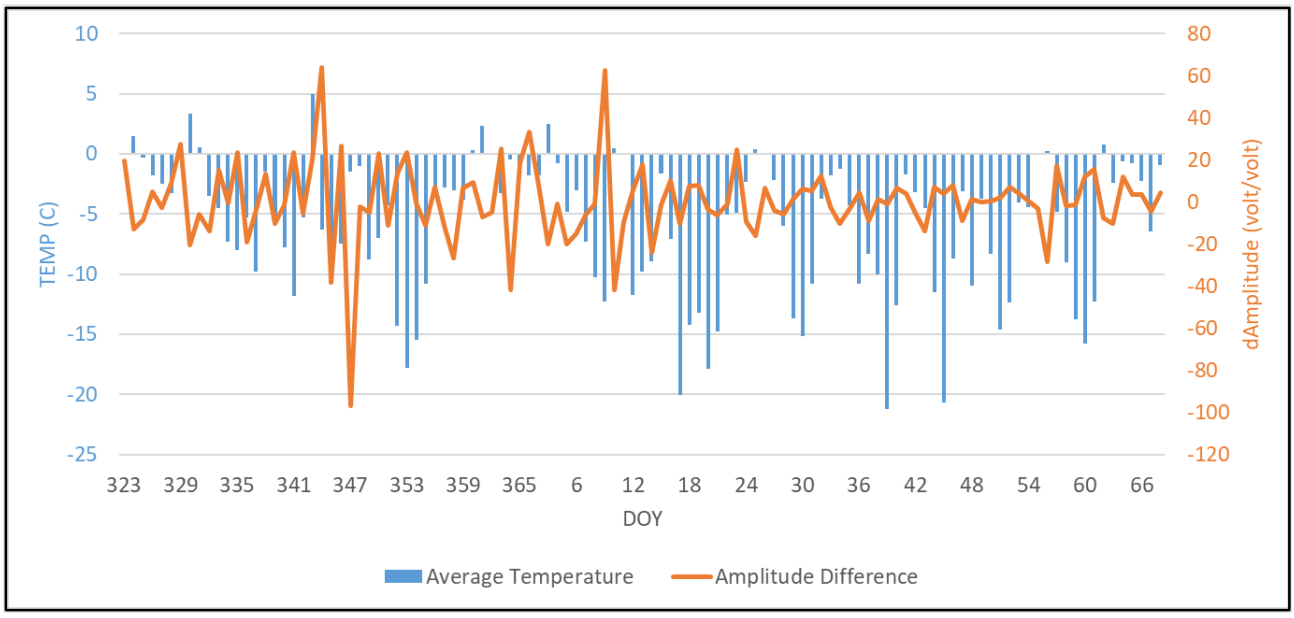

Figure 4.13. Daily SNR amplitude differences and air temperature variations.

In Figure 4.13, drops in amplitude difference are mostly connected to a temperature near or above zero on the same day or a day before or after, and almost all increments in temperature result in a drop in amplitude difference. For instance, a drop in amplitude difference can be seen on DOYs 364, 3, 10, 14, and 25, while the temperature is close to or above zero on those days. The reason for this variation is the appearance of what is believed to be wet layers inside the ice and snow columns, which increases the scattering and reduces the reflection towards the bistatic GNSS-IR antenna.

4.3.3. GNSS-IR accuracy in lake ice thickness retrieval

To examine the accuracy of GNSS-IR in estimating lake ice thickness, results of the *first frequencies* related to the 2-hour intervals are considered only over those dates with significant negative values. The reason for choosing first frequencies is the high amplitude of their SNRs and, by implication, their high level of reliability compared to the three other orders of frequencies. Moreover, the 2-hour intervals are chosen because the high density of the retrievals results in a

better assessment. In addition, dates with significant negative values are chosen for this assessment to avoid the interference of positive values, as well as the effect of near surface slush layers like those encountered on DOYs 38 and 40. The criterion for picking significant depth values is being larger than 0.5 of the ice thickness at the time of measurement.

Based on this criterion, 34 data points were chosen among 2-hour interval results, which are all related to dates with constantly cold temperatures. Figure 4.14 shows the Spearman's R correlation between ice thicknesses obtained from Stefan's equation and GNSS-IR, which is 0.68 (not significant in 5% level), with a root mean square error (RMSE) of 0.07 m and mean bias error (MBE) of -0.02 m. However, the same correlation cannot be achieved for higher frequencies since inconsistencies between those results are too much due to the low level of their amplitudes.

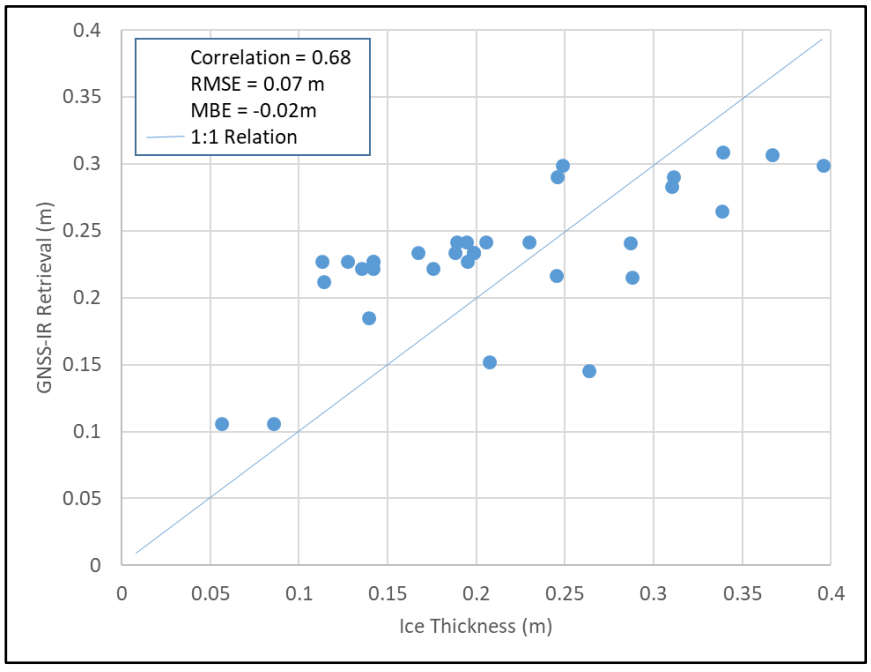

Figure 4.14. Correlation and error statistics (RMSE and MBE) of GNSS-IR retrievals compared to estimates obtained from Stefan's equation.

4.3.4. Higher frequencies in GNSS-IR

Although higher frequencies of GNSS-IR SNR have shown less relevance in retrieving ice thickness and snow depth compared to the first frequency, it is not necessarily concluded that higher frequencies are not useful in retrieving the depths of layers. As discussed in 2.3.1, even under cold conditions, a small portion of the GNSS signals is reflected from layers above the ice-water interface. For DOYs 1 to 22 as a relatively long-lasting cold period, the first and the second frequencies of the 2-hour interval SNR files were analyzed and the results are shown against the snow and ice trends in Figure 4.15. Both frequencies represent both the bottom of the ice and the top of the snowpack. The first and second frequencies interchangeably show two layers and show almost similar heights for each of those layers. Thus, one can speculate upon the efficiency of higher frequencies in retrieving the depth or level of different layers in lake ice.

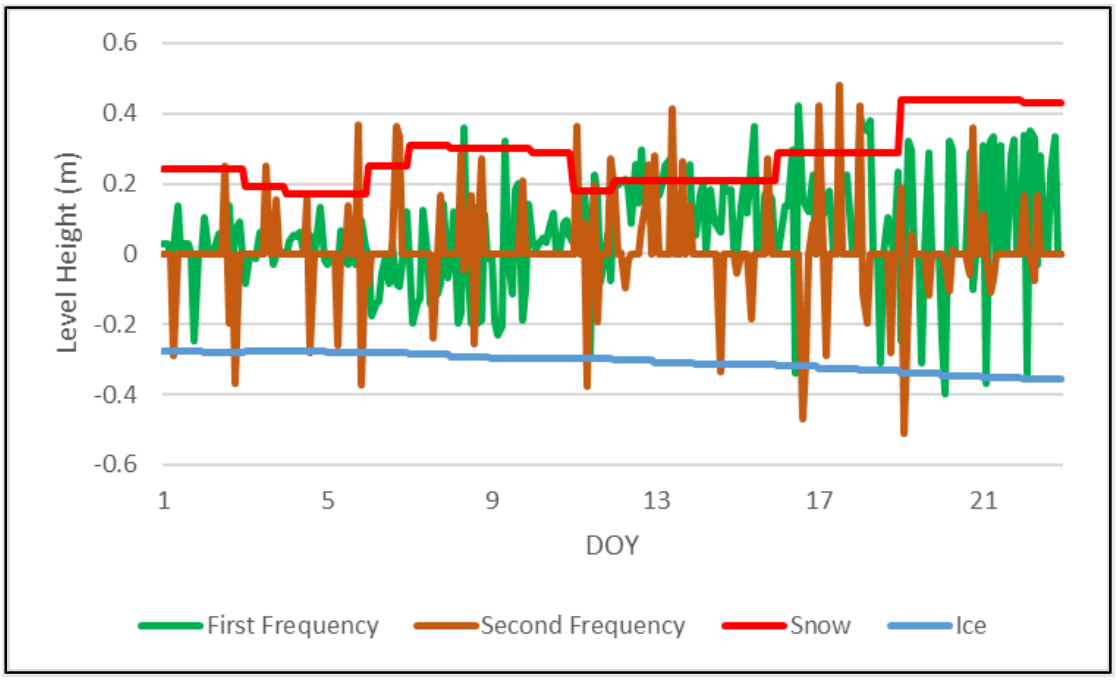

Figure 4.15. First and second frequencies results for DOYs 1 to 21 compared to ice thickness (from Stefan's equation) and snow depth (from CLIMo) trends.

It should be noted that the most part of reflected GNSS signals are LHCP, and RHCP reflected signals, which are used in this study, are only collected at lower elevation angles (5 to 25 degrees). Therefore, larger footprints and lower resolution are expected from these signals with a low penetration power. As a result, one may assume the RHCP reflected signals are considerably affected by overlaying layers, especially in warmer temperatures and wet conditions. However, upon a closer look at cold days, as shown in Figure 4.15, RHCP signals shows the potential to estimate the level of multiple overlying layers in lake ice.

4.3.5. Limitations

This study raises the question as to whether an LHCP antenna could be used as a GNSS-IR antenna to collect time series of reflected GNSS signals during an ice season. It should be noted that most GNSS missions collecting LHCP reflected signals for ice studies are classified as GNSS-R and do not collect reflected signals from a stationary location (e.g. tower). Therefore, analyzing the frequency of SNR to obtain the antenna height, as conducted in this experiment, is still an undiscovered area in lake ice thickness studies using the reflectometry approach.

Overall, the ability of the GNSS-IR technique and RHCP reflected GNSS signals in estimating the ice thickness for temperate lake ice was evaluated. One of the main attributes of mid latitude frozen lakes are the presence of wet layers happening mostly due to warm temperature or slushing at the snow-ice interface. Such conditions do not allow for the retrieval of lake ice thickness from GNSS-IR; however, during periods with constantly cold temperatures over several days, GNSS-IR shows the ability for obtaining ice thickness with the correlation of 0.68, as was also demonstrated in Chapter 3 for lakes located in the sub-Artic that experience several months with well below zero air temperatures. Otherwise, the GNSS-IR results show good agreement with GNSS retrieved heights and measured snow depth when snow is wet.

Chapter 5 –Conclusions, Limitations, and Recommendations for Future Work

This thesis has examined the potential of GNSS-IR for the retrieval of ice thickness using data acquired in two contrasting lake environments; cold sub-Arctic and mid latitude. The latter is influenced by air temperature fluctuations near the melting point of zero degrees for many days of the ice season and by the mass of snow which also promotes slushing events, resulting in wet layers detectable from GNSS-IR. The findings are promising in general and corroborate the potential of GNSS-IR approach in lake ice studies. However, it is an area of research that remains open as GNSS-IR had not yet been evaluated for ice studies.

For the sub-Artic, GNSS-IR experiments were conducted at 14 lake locations in Northwest Territories, Canada, where GNSS antennas were directly installed on the ice surface. In this experiment, the ice-water interface was determined to be the main reflective surface, and the antenna phase centre height from the ice-water interface was used to estimate the ice thickness. GNSS-IR retrievals compared favorably with manual measurements of ice thickness with a correlation of 0.66, MAE of 0.05 m, MBE of -0.01 m, and RMSE of 0.07 m.

For the mid-latitude experiment, a GNSS-IR sensor was installed on a tower by the shore of MacDonald Lake, Haliburton, Ontario, to collect reflected GNSS signals off the lake ice during the ice season 2019-2020. Although the initial plan for this research was also for the retrieval of ice thickness, warm weather conditions and fluctuating temperatures contributed to the occurrence of wet layers over and inside the snow/ice columns acting as a barrier for GNSS signals to reach to the bottom of the ice. Such conditions, which are common at mid-latitude temperate lake locations, lead to GNSS signals being received mostly from wet layers rather than the ice-water interface. However, for times during the ice season when the air temperature remains cold for

several consecutive days, the ice thickness could be retrieved with a RMSE of 0.07 m, MBE of -0.02 m, and the correlation of 0.68. Moreover, the contribution of other layers in total reflection is obtained and analyzed using LS-HE method of frequency retrieval to estimate the antenna heights from other reflective layers as well.

While GNSS-IR demonstrates potential for estimating ice thickness, it is highly dependent on the weather conditions as shown in the MacDonald Lake experiment. In other words, if the temperature is low enough to prevent slush and wet layers from forming, GNSS-IR is capable of ice thickness retrieval; whilst in case of wet snow conditions, the GNSS-IR results have propensity to imitate the snow accumulation pattern. However, even under cold conditions, a small amount of reflection is expected from other layers above the ice-water interface, and it sheds light on the potential of retrieving the depth of multiple reflective surfaces/layers, rather than only the ice-water interface.

Better results are expected from the use of an LHCP antenna as a reflectometry sensor since the main part of the reflected GNSS signals are left-handed ones. Therefore, one would anticipate signals with higher amplitudes at higher elevation angles to be reflected from lake ice leading to determining the depth of multiple layers. However, geodetic LHCP antennas with high gain are not commercially produced and, as a result, the price is higher than normal geodetic antennas ($2,500). Nonetheless, future studies should test low-gain single-frequency LHCP antennas.

In addition to ice thickness, lake ice phenology (freeze-up and break-up dates) is another element that can be studied and determined by means of GNSS-IR. Comparing the SNR amplitude of reflected signals during freeze-up in Chapter 4, one can discern ice from water as reflection from newly formed ice has shown a higher amplitude compared to open water. However, the SNR amplitude would not necessarily stay at a high value because wet layers coming after warm

conditions reduced the reflection towards the GNSS-IR antenna. Similar to the freeze-up timing, the break-up timing would be expected to be determined as well; however, the COVID-19 pandemic terminated the experiment a couple of weeks before the anticipated break-up period.

Overall, results from the two experiments (Chapters 3 and 4) provide insight into the ability of GNSS-IR for estimating lake ice thickness and determining the depth of overlaying wet layers above the ice by extracting higher orders of the SNR frequency using LS-HE method. Furthermore, the deployment of LHCP antennas could provide a wider opportunity in retrieving the depth of snow/ice layers at higher resolution and with greater accuracy.

References

Amiri-Simkooei, A (2005). Separating receiver noise and multipath effects in time series of GPS baselines using harmonic functions. Paper presented at the *ION GNSS 18th International Technical Meeting of the Satellite Division,* 1034-1045.

Amiri-Simkooei, A. R., Tiberius, C., & Teunissen, s. P. (2007). Assessment of noise in GPS coordinate time series: Methodology and results. *Journal of Geophysical Research: Solid Earth, 112*(B7).

Amiri-Simkooei, A. (2007). Least-squares variance component estimation: Theory and GPS applications, *Doctoral Thesis*. Delft University of Technology.

Amiri-Simkooei, A. R., & Asgari, J. (2012). Harmonic analysis of total electron contents time series: Methodology and results. *GPS Solutions, 16*(1), 77-88.

Amiri-Simkooei, A., & Parvazi, K. (2017). Extracting tidal frequencies of the Persian Gulf and Oman sea using multivariate least square harmonic estimation of sea level coastal height observations time series. *Journal of the Earth and Space Physics, 43*(1), 165-180.

Asgari, J., & Harmel, A. (2001). Least square spectral analysis of the GPS derived ionospheric data. Paper presented at the *Proceedings of the 2005 National Technical Meeting of the Institute of Navigation,* 716-724.

Benson, B. J., Magnuson, J. J., Jensen, O. P., Card, V. M., Hodgkins, G., Korhonen, J., Granin, N. G. (2012). Extreme events, trends, and variability in northern hemisphere lake-ice phenology (1855–2005). *Climatic Change, 112*(2), 299-323.

Bilello, M. A. (1980). Decay patterns of fast sea ice in Canada and Alaska. *IAHS Publication*, *124*, 313-326.

Bishop, G. J., Klobuchar, J. A., & Doherty, P. H. (1985). Multipath effects on the determination of absolute ionospheric time delay from GPS signals. *Radio Science, 20*(3), 388-396.

Brown, L. C., & Duguay, C. R. (2010). The response and role of ice cover in lake-climate interactions. *Progress in Physical Geography, 34*(5), 671-704.

Brown, L. C., & Duguay, C. R. (2011). The fate of lake ice in the North American arctic. *The Cryosphere, 5*(4), 869.

Brown, L. C., & Duguay, C. R. (2012). Modelling lake ice phenology with an examination of satellite-detected subgrid cell variability. *Advances in Meteorology, 2012*, 529064.

Byun, S. H., Hajj, G. A., & Young, L. E. (2002). Development and application of GPS signal multipath simulator. *Radio Science, 37*(6), 1-23.

Cardellach, E., Fabra, F., Rius, A., Pettinato, S., & D'Addio, S. (2012). Characterization of dry-snow sub-structure using GNSS reflected signals. *Remote sensing of Environment, 124*, 122-134.

Chew, C. C., Small, E. E., Larson, K. M., & Zavorotny, V. U. (2013). Effects of near-surface soil moisture on GPS SNR data: Development of a retrieval algorithm for soil moisture. *IEEE Transactions on Geoscience and Remote Sensing*, *52*(1), 537-543.

Chew, C., Shah, R., Zuffada, C., Hajj, G., Masters, D., & Mannucci, A. J. (2016). Demonstrating soil moisture remote sensing with observations from the UK TechDemoSat- 1 satellite mission. *Geophysical Research Letters, 43*(7), 3317-3324.

Chew, C., Small, E. E., & Larson, K. M. (2016). An algorithm for soil moisture estimation using GPS-interferometric reflectometry for bare and vegetated soil. *GPS Solutions, 20*(3), 525-537.

Chew, C. C., & Small, E. E. (2018). Soil moisture sensing using spaceborne GNSS reflections: Comparison of CYGNSS reflectivity to SMAP soil moisture. *Geophysical Research Letters, 45*(9), 4049-4057.

Clarizia, M. P., Zavorotny, V., & Ruf, C. S. (2015). Algorithm theoretical basis document level 2 wind speed retrieval. *University of Michigan Documents*, 148-0138.

Du, J., Kimball, J. S., Duguay, C., Kim, Y., & Watts, J. D. (2017). Satellite microwave assessment of Northern Hemisphere lake ice phenology from 2002 to 2015. *The Cryosphere, 11*, 47.

Duguay, C. R., & Lafleur, P. M. (2003). Determining depth and ice thickness of shallow sub-arctic lakes using space-borne optical and SAR data. *International Journal of Remote Sensing, 24*(3), 475-489.

Duguay, C. R., Flato, G. M., Jeffries, M. O., Ménard, P., Morris, K., & Rouse, W. R. (2003). Ice-cover variability on shallow lakes at high latitudes: Model simulations and observations. *Hydrological Processes, 17*(17), 3465-3483.

Duguay, C. R., Prowse, T. D., Bonsal, B. R., Brown, R. D., Lacroix, M. P., & Ménard, P. (2006). Recent trends in Canadian lake ice cover. *Hydrological Processes, 20*(4), 781-801.

Duguay, C. R., Bernier, M., Gauthier, Y., & Kouraev, A. (2015). Remote sensing of lake and river ice. In *Remote Sensing of the Cryosphere*, 273-306.

Engram, M., Anthony, K. W., Meyer, F. J., & Grosse, G. (2013). Characterization of L-band synthetic aperture radar (SAR) backscatter from floating and grounded thermokarst lake ice in arctic Alaska. *The Cryosphere, 7*(6), 1741-1752. doi:10.5194/tc-7-1741-2013

Fabra, F., Cardellach, E., Rius, A., Ribo, S., Oliveras, S., Nogués-Correig, O., Rivas, M. B., Semmling, M., & D'Addio, S. (2011). Phase altimetry with dual polarization GNSS-R over sea ice. *IEEE Transactions on Geoscience and Remote Sensing, 50*(6), 2112-2121.

Foti, G., Gommenginger, C., Jales, P., Unwin, M., Shaw, A., Robertson, C., & Rosello, J. (2015). Spaceborne GNSS reflectometry for ocean winds: First results from the UK TechDemoSat-1 mission. *Geophysical Research Letters, 42*(13), 5435-5441.

Garrison, J. L., Komjathy, A., Zavorotny, V. U., & Katzberg, S. J. (2002). Wind speed measurement using forward scattered GPS signals. *IEEE Transactions on Geoscience and Remote Sensing, 40*(1), 50-65.

Georgiadou, Y., & Kleusberg, A. (1988). On carrier signal multipath effects in relative GPS positioning. *Manuscripta Geodaetica, 13*(3), 172-179.

Gleason, S. (2006). Remote sensing of ocean, ice and land surfaces using bistatically scattered GNSS signals from low earth orbit. *Doctoral Dissertation,* University of Surrey.

Gunn, G. E., Duguay, C. R., Brown, L. C., King, J., Atwood, D., & Kasurak, A. (2015). Freshwater lake ice thickness derived using surface-based X-and Ku-band FMCW scatterometers. *Cold Regions Science and Technology, 120*, 115-126.

Heron, R., & Woo, M. (1994). Decay of a high arctic lake-ice cover: Observations and modelling. *Journal of Glaciology, 40*(135), 283-292.

Hoekstra, M. (2018). Toward automated ice-water classification on large northern lakes using RADARSAT-2 synthetic aperture radar imagery. *Master's Thesis*, University of Waterloo.

Hofmann-Wellenhof, B., Lichtenegger, H., & Wasle, E. (2007). GNSS–global navigation satellite systems: GPS, GLONASS, Galileo, and more. *Springer Science & Business Media*.

Jacobson, M. D. (2015). Potential for estimating the thickness of freshwater lake ice by GPS interferometric reflectometry. *Journal of Geography and Geology, 7*(1), 10.

Jeffries, M. O., Morris, K., & Liston, G. E. (1996). A method to determine lake depth and water availability on the north slope of Alaska with spaceborne imaging radar and numerical ice growth modelling. *Arctic, ,* 367-374.

Jeffries, M. O., Morris, K., & Kozlenko, N. (2005). Ice characteristics and processes, and remote sensing of frozen rivers and lakes. In *Remote Sensing in Northern Hydrology: Measuring Environmental Change*, 63.

Kang, K., Duguay, C. R., Howell, S. E., Derksen, C. P., & Kelly, R. E. (2010). Sensitivity of AMSR-E brightness temperatures to the seasonal evolution of lake ice thickness. *IEEE Geoscience and Remote Sensing Letters, 7*(4), 751-755.

Kheyrollah Pour, H., Duguay, C. R., Martynov, A., & Brown, L. C. (2012). Simulation of surface temperature and ice cover of large northern lakes with 1-D models: A comparison with MODIS satellite data and in situ measurements. *Tellus A: Dynamic Meteorology and Oceanography, 64*(1), 17614.

Knoll, L. B., Sharma, S., Denfeld, B. A., Flaim, G., Hori, Y., Magnuson, J. J., Straile, D., & Weyhenmeyer, G. A. (2019). Consequences of lake and river ice loss on cultural ecosystem services. *Limnology and Oceanography Letters, 4*(5), 119-131.

Komjathy, A., Maslanik, J., Zavorotny, V. U., Axelrad, P., & Katzberg, S. J. (2000). (2000). Sea ice remote sensing using surface reflected GPS signals. Paper presented at the *IGARSS 2000. IEEE 2000 International Geoscience and Remote Sensing Symposium. Taking the Pulse of the Planet: The Role of Remote Sensing in Managing the Environment. Proceedings (Cat. no. 00CH37120), , 7* 2855-2857.

Larson, K. M., Braun, J. J., Small, E. E., Zavorotny, V. U., Gutmann, E. D., & Bilich, A. L. (2009). GPS multipath and its relation to near-surface soil moisture content. *IEEE Journal of Selected Topics in Applied Earth Observations and Remote Sensing, 3*(1), 91-99.

Larson, K. M., Small, E. E., Gutmann, E., Bilich, A., Axelrad, P., & Braun, J. (2008). Using GPS multipath to measure soil moisture fluctuations: Initial results. *GPS Solutions, 12*(3), 173-177.

Larson, K. M. (2016). GPS interferometric reflectometry: Applications to surface soil moisture, snow depth, and vegetation water content in the western united states. *Wiley Interdisciplinary Reviews: Water, 3*(6), 775-787.

Larson, K. M., MacFerrin, M., & Nylen, T. (2020). Brief communication: Update on the GPS reflection technique for measuring snow accumulation in Greenland. *The Cryosphere Discussion, 2020*, 1-9. doi:10.5194/tc-2019-303

Lenormand, F., Duguay, C. R., & Gauthier, R. (2002). Development of a historical ice database for the study of climate change in Canada. *Hydrological Processes, 16*(18), 3707-3722.

Li, W., Cardellach, E., Fabra, F., Rius, A., Ribó, S., & Martín-Neira, M. (2017). First spaceborne phase altimetry over sea ice using TechDemoSat-1 GNSS-R signals. *Geophysical Research Letters, 44*(16), 8369-8376.

Li, W., Cardellach, E., Fabra, F., Ribó, S., & Rius, A. (2019). Assessment of spaceborne GNSS-R ocean altimetry performance using CYGNSS mission raw data. *IEEE Transactions on Geoscience and Remote Sensing, 58*(1), 238-250.

Li, W., Cardellach, E., Fabra, F., Ribó, S., & Rius, A. (2020). Measuring Greenland ice sheet melt using spaceborne GNSS reflectometry from TechDemoSat- 1. *Geophysical Research Letters, 47*(2), e2019GL086477.

Liu, L., & Larson, K. M. (2018). Decadal changes of surface elevation over permafrost area estimated using reflected GPS signals. *Cryosphere, 12*(2)

Magnuson, J. J. (2001). Historical trends in lake and river ice cover in the Northern Hemisphere (vol 290, pg. 1743, 2000). *Science, 291*(5502), 254.

Martin-Neira, M. (1993). A passive reflectometry and interferometry system (PARIS): Application to ocean altimetry. *ESA Journal, 17*, 331-355.

Mashburn, J. R. (2019). Analysis of GNSS-R observations for altimetry and characterization of earth surfaces. *Doctoral Dissertation*, University of Colorado at Boulder.

Mayers, D., & Ruf, C. (2018). Measuring ice thickness with CYGNSS altimetry. Paper presented at the *IGARSS 2018-2018 IEEE International Geoscience and Remote Sensing Symposium*, 8535-8538.

Murfitt, J., & Brown, L. C. (2017). Lake ice and temperature trends for Ontario and Manitoba: 2001 to 2014. *Hydrological Processes, 31*(21), 3596-3609.

Murfitt, J. C. (2018). Monitoring ice phenology and characteristics in mid-latitudes using RADARSAT-2, *Master's Thesis*, University of Toronto.

Murfitt, J. C., Brown, L. C., & Howell, S. E. (2018). Estimating lake ice thickness in central Ontario. *PloS One, 13*(12).

Nievinski, F. G., & Larson, K. M. (2014). Forward modeling of GPS multipath for near-surface reflectometry and positioning applications. *GPS Solutions, 18*(2), 309-322.

Prowse, T., Alfredsen, K., Beltaos, S., Bonsal, B. R., Bowden, W. B., Duguay, C. R., Korhola, A., McNamara, J., Vincent, W. F., Vuglinsky, V., & Vuglinsky, V. (2011). Effects of changes in arctic lake and river ice. *Ambio, 40*(1), 63-74.

Rius, A., Aparicio, J. M., Cardellach, E., Martín-Neira, M., & Chapron, B. (2002). Sea surface state measured using GPS reflected signals. *Geophysical Research Letters*, *29*(23), 37-4.

Roesler, C., & Larson, K. M. (2018). Software tools for GNSS interferometric reflectometry (GNSS-IR). *GPS Solutions, 22*(3), 80.

Rouse, W. R., Binyamin, J., Blanken, P. D., Bussières, N., Duguay, C. R., Oswald, C. J., Schertzer, W. M., & Spence, C. (2008). The influence of lakes on the regional energy and water balance of the central Mackenzie River basin. *Cold Region Atmospheric and Hydrologic Studies: The Mackenzie GEWEX Experience* (pp. 309-325) Springer.

Samama, N. (2008). Global positioning: Technologies and performance. *John Wiley & Sons*.

Stefan, J. (1890). On the theory of ice formation, with particular regard to ice formation in the polar sea. *Sitz.Ber.Kais.Akad.Wiss.Wien, 98*, 965-983.

Strandberg, J., Hobiger, T., & Haas, R. (2017). Coastal sea ice detection using ground-based GNSS-R. *IEEE Geoscience and Remote Sensing Letters, 14*(9), 1552-1556.

Ulaby, F. T., Moore, R. K. & Fung, A. K. (1981). Microwave Remote Sensing: Active and Passive, Volume 1. *Addison-Wesley*.

Vey, S., Güntner, A., Wickert, J., Blume, T., & Ramatschi, M. (2016a). Long-term soil moisture dynamics derived from GNSS interferometric reflectometry: A case study for Sutherland, South Africa. *GPS Solutions, 20*(4), 641-654.

Williams, G. P. (1965). Correlating freeze-up and break-up with weather conditions. *Canadian Geotechnical Journal, 2*(4), 313-326.

Wu, X., Jin, S., & Chang, L. (2018). Monitoring bare soil freeze–thaw process using GPS-interferometric reflectometry: Simulation and validation. *Remote Sensing, 10*(1), 14.

Xu, G., & Xu, Y. (2016). GPS: Theory, algorithms and applications. *Springer*.

Yueh, S. H., Xu, X., Shah, R., Kim, Y., Garrison, J. L., Komanduru, A., & Elder, K. (2017). Remote sensing of snow water equivalent using coherent reflection from satellite signals of opportunity: Theoretical modeling. *IEEE Journal of Selected Topics in Applied Earth Observations and Remote Sensing, 10*(12), 5529-5540.

Zavorotny, V. U., Gleason, S., Cardellach, E., & Camps, A. (2014). Tutorial on remote sensing using GNSS bistatic radar of opportunity. *IEEE Geoscience and Remote Sensing Magazine, 2*(4), 8-45.

Zhang, S., Roussel, N., Boniface, K., Ha, M. C., Frappart, F., Darrozes, J., Baup, F., & Calvet, J. (2017). Use of reflected GNSS SNR data to retrieve either soil moisture or vegetation height from a wheat crop. *Hydrology and Earth System Sciences, 21*(9), 4767.

Zhou, W., Liu, L., Huang, L., Yao, Y., Chen, J., & Li, S. (2019). A new GPS SNR-based combination approach for land surface snow depth monitoring. *Scientific Reports, 9*(1), 1-20.